Quantifying local-scale dust emission from the Arabian Red Sea coastal plain

Anatolii Anisimov[1], Weichun Tao[1#], Georgiy Stenchikov[1], Stoitchko Kalenderski[1], P. Jish Prakash[1], Zong-Liang Yang[2], Mingjie Shi[2*]

[1]King Abdullah University of Science and Technology (KAUST), Physical Science and Engineering Division (PSE), Thuwal, 23955-6900, Saudi Arabia
[2]The University of Texas at Austin, Jackson School of Geosciences, Department of Geological Sciences, Austin, TX 78712, USA
[#]Now at Policy Research Center of Environment and Economy, Ministry of Environmental Protection, Beijing, 100029, People's Republic of China
[*]Now at Jet Propulsion Laboratory, California Institute of Technology, 4800 Oak Grove Drive, Pasadena, CA 91109, USA

Correspondence to: Georgiy Stenchikov (georgiy.stenchikov@kaust.edu.sa)

Abstract. Dust plumes emitted from the narrow Arabian Red Sea coastal plain are often observed on satellite images and felt in local population centers. Despite its relatively small area, the coastal plain could be a significant dust source, however, its effect is not well quantified as it is not well approximated in global or even regional models. In addition, because of close proximity to the Red Sea, a significant amount of dust from the coastal areas could be deposited into the Red Sea and serve as a vital component of the nutrient balance of marine ecosystems.

In the current study, we apply the off-line Community Land Model version 4 (CLM4) to better quantify dust emission from the coastal plain during the period of 2009 – 2011. We verify the spatial and temporal variability of model results using independent weather station reports. We also compare the results with the MERRA Aerosol Reanalysis (MERRAero). We show that the best results are obtained with 1-km model spatial resolution and dust source function based on Meteosat Second Generation Spinning Enhanced Visible and InfraRed Imager (SEVIRI) measurements. We present the dust emission spatial pattern, estimates of seasonal and diurnal variability of dust event frequency and intensity, and discuss the emission regime in the major dust generation hot spot areas. We demonstrate the contrasting seasonal dust cycles in the northern and southern parts of the coastal plain and discuss the physical mechanisms responsible for dust generation.

This study provides the first estimates of the fine-scale spatial and temporal distribution of dust emissions from the Arabian Red Sea coastal plain constrained by the MERRAero reanalysis and short-term WRF-Chem simulations. The estimate of total dust emission from the coastal plain, tuned to fit emissions in MERRAero, is 7.5±0.5 Mt a^{-1}. Small inter-annual variability indicates that the study area is a stable dust source. The mineralogical composition analysis shows that the coastal plain generates around 76±5 Kt of iron oxides and 6±0.4 Kt of phosphorus annually. Over 65 % of dust is emitted from the northern part of the coastal plain.

1 Introduction

The mineral dust has a significant impact on climate at regional and global scales (Choobari et al., 2014; Miller et al., 2014; Shao et al., 2011a). Dust particles also play an important role in soil and forest biogeochemistry. Atmospheric deposition is a vital component of the nutrient balance of marine ecosystems (Jickells et al., 2005; Mahowald et al., 2005; Nickovic et al., 2012 and references therein; Schulz et al., 2012). Dust air-pollution also affects human health, increasing the risk of human morbidity and mortality (Morman and Plumlee, 2014).

The exploration of dust generation and transport, as well as climatology and seasonality of the dust cycle in the Arabian Peninsula, is gaining increased attention in recent years (Hamidi et al., 2013; Hamidi et al., 2014; Kalenderski and Stenchikov, 2016; Kalenderski et al., 2013; Notaro et al., 2013; Notaro et al., 2015; Prakash et al., 2015; Rezazadeh et al., 2013; Shalaby et al., 2015; Shi et al., 2016; Yu et al., 2013; Yu et al., 2015; Alobaidi et al., 2016). Along with a strong climate effect, dust outbreaks in this region affect the nutrient balance of the semi-enclosed Red and Arabian Seas. For example, it was shown that the passage of major dust storms over the Arabian Sea causes chlorophyll blooming (Singh et al., 2008). The Red Sea, bordered by the Sahara and Arabian deserts, and with little or no river discharge and infrequent flash floods from land, is highly oligotrophic, especially in the northern part, rendering nutrients coming from the Indian Ocean almost unobtainable (Acker et al., 2008; Chase et al., 2011; Weikert, 1987). Therefore, atmospheric dust and gaseous depositions are especially important as nutrient supplies for the Red Sea (Kalenderski et al., 2013; Prakash et al., 2015).

Although previous studies indicate that dust outbreaks are most frequent over the eastern sector of Saudi Arabia (Barkan et al., 2004; Goudie and Middleton, 2006; Prospero et al., 2002; Shalaby et al., 2015; Washington et al., 2003), satellite images and ground observations show that there is a zone of increased dust activity in the western part of the Arabian Peninsula (Ackerman and Cox, 1989; Furman, 2003; Ginoux et al., 2012; Shao, 2008; Shao et al., 2011a; Walker et al., 2009; Yu et al., 2013). Located next to the Red Sea, the narrow coastal plain could make a significant contribution to the overall amount of dust depositing to the sea, transporting iron, phosphorus, and nitrogen. However, despite the importance of this source area for the nutrient balance of the Red Sea, no specific studies have been focused on the semi-desert coastal region and no estimates of the amount of dust emitted from these areas have been made yet, partly due to the scarcity of observations and partly because the narrow coastal plain is a subgrid area in most global and even regional modeling studies.

The concentration of dust particles in the atmosphere depends on small-scale emission processes, which are spatially heterogeneous and involve complex nonlinear interactions controlled by meteorological conditions and properties of land surfaces. As the measurement of emission in field conditions is extremely difficult, numerical models are the principal tools for dust emission evaluation. At the same time, the results from the AeroCom intercomparison project for atmospheric models that comprise aerosol components (Huneeus et al., 2011) suggest large discrepancies in model estimates of global dust emission and deposition up to a factor of 10. As global models can not approximate fine-scale circulations well regional

uncertainties in dust emissions are expected to be even higher. Due to the relatively small area and complex terrain structure of the western Arabian coastal plain, large-scale and even mesoscale models are not able to reproduce the dust emission processes here with the desired accuracy. Even for similar meteorological conditions, a number of studies reported substantial differences in dust fluxes predicted by different models, indicating the model deficiencies in accounting for fine-scale features such as soil texture and surface vegetation cover (Ginoux et al., 2012; Kang et al., 2011; Koven and Fung, 2008; Prospero et al., 2002; Shao, 2008; Textor et al., 2006; Todd et al., 2008; Zender et al., 2003b). Raupach and Lu (2004) identified key challenges in modeling wind erosion related to the representation of land surface processes, including the fidelity of parameterizations and the availability of high-resolution input data for dust generation calculations. Therefore, to obtain reliable estimates of dust emissions, especially in such highly heterogeneous regions as the Arabian Red Sea coastal plain, fine-resolution surface information is required.

Recently, satellite-derived high resolution datasets of surface properties have emerged and provided an opportunity for improving dust emission calculations (Bullard et al., 2011; Ginoux et al., 2012; Kang et al., 2011; Knippertz and Todd, 2012; Pérez et al., 2011; Shao et al., 2011a). For example, Kim et al. (2013) and Hamidi et al. (2014), using a dynamic vegetation dataset, enabled a simple dust emission scheme to account for the control of seasonally varying vegetation cover on dust emission, which is usually accounted for in more advanced schemes (Bullard et al., 2011; Mahowald et al., 2006; Zender et al., 2003a). Menut et al. (2013) reported that the State Soil Geographic Database (STATSGO-FAO), remapped from the Food and Agriculture Organization of the United Nations (FAO) two-layer 5-minute global soil texture dataset (Nickovic et al., 2012) provides realistic spatial patterns of dust emission for the Middle East and North Africa. Shi et al. (2016) discussed the impact of the satellite-derived vegetation dataset on patterns and intensity of dust emission in the Arabian Peninsula. Many studies have been devoted to accurately locating dust source regions using different criteria, accounting for sediment availability and erodibility due to geographic influences, and applying satellite datasets to define so-called source functions (Ginoux et al., 2012; Kim et al., 2013; Parajuli et al., 2014; Walker et al., 2009; Zender et al., 2003b).

In this study, we focus on dust emission from a relatively small local area: the narrow semi-desert western coast of the Arabian Peninsula. We employ the high-resolution Community Land Model version-4 (CLM4) with the Dust Entrainment and Deposition (DEAD) module to conduct simulations for the three-year span of 2009–2011. Our principle objective is to conduct multi-year emission simulations and study fine-scale dust generation areas, evaluate the temporal variability of dust emissions and assess the mineralogical composition of local dust, as a potential source of nutrients for the Red Sea. We utilize the fine-scale input datasets of soil characteristics derived from satellite-based instruments and examine the model's sensitivity to their horizontal resolution. Using high-frequency satellite measurements, we also calculate and apply the dust emission statistical source function and demonstrate the benefits of using high-resolution inventories.

We compare the results with independent weather code and visibility reports from meteorological stations. Although these data are indirectly related to local dust emissions and cannot be applied for accurate model validation, they may provide

valuable information and serve as a reference for determining optimal model configuration (Engelstaedter et al., 2006; Tegen, 2003). We also compare (and calibrate) our dust emission estimates with MERRA Aerosol Reanalysis (MERRAero) (Buchard et al., 2016), a recent reanalysis product that includes an aerosol model component and has the highest spatial resolution compared with analogous products, and with short-term Weather Research and Forecasting model coupled with Chemistry (WRF-Chem) simulations.

Marine productivity is largely limited by the availability of iron (Mahowald, 2009), which in turn depends on the solubility of iron-containing compounds in seawater. It has been shown that aerosol source mineralogy is a crucial factor for iron content and solubility as well as aging in the course of particle transport (Baker and Croot, 2010 and references therein). Together with iron, both phosphorus and nitrogen also frequently limit marine productivity (Okin et al., 2011). To evaluate the possible mineralogical composition of nutrients deposited in the Red Sea from local sources, we apply the global dataset of soil texture and mineral composition, GMINER30, developed by Nickovic et al. (2012). We assume that the mineral composition and size fractioning of the emitted dust are the same as those of the parent soil. This assumption does not always hold (Claquin et al., 1999; Perlwitz et al., 2015). Moreover, airborne dust changes its size distribution and mineralogical composition during its life cycle. Nevertheless, due to the short pathway from the coastal plain to the sea, the atmospheric processing of dust particles from this closely located source is less important compared to those subjected to long-range transport, and our assessment may serve as an initial estimate of the mineralogical composition of dust particles deposited to the Red Sea.

The rest of the article is organized as follows: In Sect. 2, we present the model description and characterize the study domain and observational datasets. In Sect. 3, we describe numerical experiments, examine model sensitivity to land surface datasets and compare results with station observations. A detailed analysis of dust generation and its spatial-temporal variability is conducted in Sect. 4. We summarize our results and draw conclusions in Sect. 5.

2 Data and methods

2.1 CLM4 model and meteorological forcing

We perform the numerical experiments using the off-line CLM4 (Lawrence et al., 2011; Oleson et al., 2010) implemented with the DEAD module (Zender et al., 2003a). CLM4 is the land surface model used with the global Community Earth System Model (CESM) (Hurrell et al., 2013), and some other regional models [i.e. Regional Climate Model (RegCM4) (Wang et al., 2016) and Weather Research and Forecasting (WRF) (Zhao et al., 2016)]. CLM4 calculates turbulent fluxes of momentum, heat, and water vapor from the surface into the atmosphere, interaction of solar and thermal radiation with soil and vegetation, and heat and moisture fluxes in soils. CLM4 also simulates vegetation processes. The off-line version of CLM4 can be run at a finer spatial resolution than driving meteorological fields to account for high heterogeneity of land

surface. Additionally, some soil characteristics in CLM4 can be prescribed, instead of being calculated within the model. In this study, we turn off the transient land cover change calculations and the dynamic global vegetation model to conduct historical simulations using observed high-resolution satellite land cover and vegetation datasets instead.

CLM4 is forced by meteorological fields including the wind, surface pressure, precipitation, temperature, and incoming solar and thermal radiation. The driving meteorological fields for CLM4 are provided by the WRF model (Skamarock et al., 2008) run at a 10 km × 10 km resolution over the Arabian Peninsula (8.06° N–34.6° N, 30.3° E–60.9° E) for the period of 2009–2011. The domain completely covers the Arabian Red Sea coastal area (Fig. 1). The WRF configuration used in our simulations is detailed in Table 1. It generally follows default recommendations from the user guide and is identical to that used in (Jiang et al., 2011).

2.2 Dust generation

The DEAD module (Zender et al., 2003a) is designed to calculate dust emission at both local and global scales, generally following the microphysical and micrometeorological model of dust mobilization developed by Marticorena and Bergametti (1995). Soil moisture, vegetation properties, land use, and soil texture data needed to drive DEAD are provided by CLM4. DEAD falls into the category of intermediate complexity models that are more sophisticated than simple bulk mobilization schemes (Tegen and Fung, 1994) and not as complex and calculation-heavy as fully microphysical schemes (Marticorena and Bergametti, 1995; Shao, 2004; Shao et al., 2011b). Intermediate complexity models use microphysical parameterizations where possible, but make simplifying assumptions and use empirical coefficients to shortcut complex calculations (Zender et al., 2003a). The total vertical mass flux of dust F (kg m^{-2} s^{-1}), generated from the ground into the atmosphere is calculated using the following equation:

$$F = TSf_m Q_s \sum_{j=1}^{4} \alpha_j M_j, \quad (1)$$

where T is a spatially uniform tuning constant that controls the average emission rate (see Sect. 2.4).

The f_m parameter is a grid cell fraction of soils suitable for dust mobilization. It depends on the land fraction of bare soil (which is calculated dynamically depending on soil conditions), the plant function type (PFT), leaf area index (LAI), stem area index (SAI), and top soil layer water content, calculated within CLM4.

The α_j coefficients are sandblasting mass efficiencies for each of the four dust transport size bins j. They depend on the mass fraction of clay particles (CLY) in the soil, which is defined by SOILPOP30, a 30-second soil population dataset developed by Nickovic et al. (2012) from STATSGO-FAO. This soil dataset is widely used in dust-related studies (e.g., Menut et al., 2013).

M_j is a mass fraction of dust size bin j. The size bins approximate particles with diameters from 0.1 μm to 1 μm, from 1 μm to 2.5 μm, from 2.5 μm to 5.0 μm and from 5 μm to 10 μm. In the original model formulation, the emission flux is calculated separately for each size bin. Here, we consider total emitted dust mass and therefore, sum up fluxes from all the bins in equation (1).

Q_s is the total horizontally saltating mass flux (kg m^{-2} s^{-1}). It is proportional to the third power of wind friction velocity u_{*s} (m s^{-1}) when it exceeds threshold velocity u_{*t}:

$$Q_s = \begin{cases} \frac{c_s \rho_{atm} u_{*s}^3}{g}\left(1 - \frac{u_{*t}}{u_{*s}}\right)\left(1 + \frac{u_{*t}}{u_{*s}}\right)^2, & \text{for } u_{*s} > u_{*t}, \\ 0, & \text{for } u_{*s} \le u_{*t} \end{cases} \quad (2)$$

where c_s is the saltation constant equal to 2.61, ρ_{atm} is the atmospheric density (kg m^{-3}), and g is the acceleration of gravity (m s^{-2}). Saltation wind friction velocity u_{*s} is calculated from wind friction velocity u_* (m s^{-1}) accounting for the Owen effect of increasing u_* during saltation (Zender et al., 2003a). Threshold friction velocity u_{*t} is calculated within CLM4 as a function of surface roughness and soil moisture.

S is a spatially varying dimensionless dust emission source function. It has a sense of soil erodibility and accounts for the susceptibility of soil to wind erosion (Webb and Strong, 2011). In the default CLM4 configuration S = 1, assuming that the emission is calculated based on winds and available surface and soil properties only. However, it has been reported recently that the models based on purely physical properties of soils represent quite inaccurate spatial patterns of dust emission, especially on the regional scale (Huneeus et al., 2011; Knippertz and Todd, 2012). This is caused by the deficiencies of parameterizations and inaccurate input information. Thus, the source function S is introduced to improve the spatial distribution of dust emission simulations.

Different approaches have been discussed and a number of principles to calculate the source function recently introduced (Kim et al., 2013; Parajuli et al., 2014; Walker et al., 2009). Ginoux et al. (2001) proposed calculating the source function based on a topographic approach, assuming that the areas with topographic depressions are the most probable locations for sediments to accumulate. The geomorphic source function (Zender et al., 2003b) is based on the assumption that dust emission is likely to occur from areas of potential runoff collection. Similar to the topographic source function, it only depends on elevation. Another family of source functions is instead based on observations (mostly remote sensing), assuming that the most active dust source areas are those where airborne dust is more frequently observed. The statistical source function introduced by Ginoux et al. (2010) and Ginoux et al. (2012) uses Moderate Resolution Imaging Spectroradiometer (MODIS) estimates of aerosol optical depth and land cover data to identify the dust source areas.

In this study, we calculate source function using the dust aerosol optical depth (AOD_D) product developed by (Brindley and Russell, 2009) and (Banks and Brindley, 2013), based on high-frequency measurements from the Meteosat Second

Generation Spinning Enhanced Visible and InfraRed Imager (SEVIRI) instrument. The SEVIRI instrument is located on board the Meteosat-9 geostationary satellite and provides measurements every 15 minutes (Brindley and Russell, 2009; Banks and Brindley, 2013), much more frequently than MODIS. SEVIRI measurements were recently utilized to analyze dust sources in Northern Africa (Schepanski et al., 2012; Evan et al., 2015). To calculate the source function we adopt the frequency method, first proposed by Prospero et al. (2002), and later used in a number of other studies (Ginoux et al., 2010, Ginoux et al., 2012, Schepanski et al., 2012). It assumes that the intensity of a dust source is proportional to the frequency of occurrence of atmospheric dust:

$$S = N\,(AOD_D > AOD_t) \,/\, N\,(AOD), \quad (3)$$

where statistical source function S is defined in each location as a ratio of the number of events $N\,(AOD_D > AOD_t)$ when dust-caused AOD_D exceeds the threshold value AOD_t, to the total number of observations $N\,(AOD)$. The threshold is meant to filter out background dust and is usually chosen empirically (Schepanski et al., 2012). We have tested the thresholds in the range of 0.8 – 1.15 and found that the spatial patterns of the source functions are quite similar. The chosen threshold value of 1.12 is larger than the one used in the global study (Ginoux et al., 2012) but comparable to regional studies of Saharan dust sources (Schepanski et al., 2012). The choice of relatively large threshold was motivated by several reasons. First, the background dust AOD in Arabian Peninsula is much higher than globally observed one. Second, SEVIRI was shown to overestimate AOD under high humidity conditions and low dust loadings that are the case for the Red Sea coastal plain (Banks et al., 2013). Overall, this larger threshold allows us to better represent intensive dust sources, in contrast, e.g. to (Ginoux et al., 2010; Ginoux et al., 2012) that aimed at capturing and classifying smaller sources. Below we show that the source function based on high-frequency measurements significantly improves the simulation results.

2.3 Observations, metrics and an overview of the study area

The targeted study area is the eastern coast of the Red Sea in western Saudi Arabia. It is shown in Fig. 1a bounded by a solid red line. The coastal area has the historical name of Tihamah. It covers both plain and hill landscapes, from the Tihamat Al-Hejaz (northern part) and Tihamat ‘Asir (southern part) coastal plains to the Scarp Mountains of Midyan, Ash Shifa’ and Asir (Edgell, 2006). The land cover, precipitation, and surface wind speed are highly heterogeneous in this narrow (on average 100 km wide) area. In the eastern part of the coastal plain, closer to the mountain area, the land is covered by more or less continuous shrubs and steppe vegetation due to higher precipitation (see Fig. 1c–e). In the northern coastal plain vegetation cover is sparser (Fig. 1f) as the annual precipitation is only 50 mm. Southward, in most of the piedmonts, annual rainfall of 100–200 mm supports denser vegetation cover (Vincent, 2008). Infrequent extreme precipitation events that cause flash floods in western Saudi Arabia (de Vries et al., 2016 and references therein) lead to accumulation of sediments in the coastal low-land areas.

The Red Sea environment has been identified as a zone of complex wind circulation (Langodan et al., 2014). Due to the strong land-sea diurnal temperature contrasts, land and sea breezes persist through the entire year. The large-scale circulation systems interact with breezes and are reinforced by orographic structures, which create a complex pattern of mesoscale circulation. The most prominent mesoscale feature of the Red Sea is the Tokar Gap jet on the western coast (Davis et al., 2015 and references therein). Westward-blowing mesoscale jets also exist on the eastern coast (Gille and Llewellyn Smith, 2014; Jiang et al., 2009). These jets originate mostly in Winter due to the cold/dry air outbreaks from the central Arabian plateau and channel through a series of mountain gaps. They may last for several days and have a prominent diurnal cycle. The jets, along with the breezes, cause small-scale dust updrafts in the coastal area. The generated dust plumes are sometimes observed by satellites over the Red Sea. For example, a dust storm with narrow dust plumes caused by the jet winds captured by MODIS/TERRA at 7:45 UTC on 14 January 2009 is shown in Fig. 1b.

In order to cover the study area, we run the CLM4 model over the two rectangular domains shown in Fig. 1a. Also shown are the meteorological observation stations that are used in the current study. We use hourly data from the Integrated Surface Dataset (ISD) developed by the National Climatic Data Center (NCDC) (Smith et al., 2011). We selected 15 stations in Saudi Arabia and 1 station in Jordan inside the CLM4 domains with continuous observation records for 2009–2011. The stations provide meteorological observations including weather code and visibility reports. The automated visibility measurement and manned weather code observation are reported on an hourly basis, but the weather code is only present when visibility reduces to below 10000 m. Otherwise, just a constant visibility of 10000 m is reported (indicating fair weather). The weather codes that correspond to the presence of dust are 06 – dust in suspension, 07 – dust raised, 08 – dust whirl, 09, 30 to 35 – dust storm. Most of the weather stations (except that in Makkah) are located on the site of regional or international airports, thus the data archive was primarily assembled from SYNOP or METAR/SPECI weather reports (Smith et al., 2011).

Although the station visibility measurements are only indirectly related to the amount of locally emitted dust, they are one of the most relevant data sources for assessing dust emission fluxes in the absence of other observations. These data are frequently used in dust-related studies. For example, the present weather code reports from meteorological records have been used for evaluation of dust event frequency and dust climatology (Cowie et al., 2014; Goudie and Middleton, 2006; Hamidi et al., 2014; Notaro et al., 2013; Shao and Dong, 2006; Wang et al., 2011; Yu et al., 2013). In some other studies, these observations were used to derive soil erodibility fields (Shao, 2008). The parameterization formula for assessing near-surface dust concentration based on visibility measurement has also been proposed (Camino et al., 2015 and references therein; Rezazadeh et al., 2013; Shao et al., 2003). Mahowald et al. (2007) used the station visibility measurements to study dust sources and stated that visibility-derived observations should better capture the temporal variability of surface dust fluxes compared to AOD measurements. But still, these data cannot serve as a quantitative measure of model performance, being non-automated (in the case of weather code), and being highly influenced by remote dust transport, the presence of water

vapor, and dust physical properties and composition (Shao, 2008). Another limitation of station observations is a weak sensitivity to low and moderate reductions in visibility that is only reported and complemented by the weather code when it drops below 10000 m. Camino et al. (2015) also note that clear skies are often reported under hazy atmospheric conditions when dust is present. Thus we do not expect out analysis to give an absolute assessment of model emissions, but to allow comparison of different model configurations.

We apply several metrics to compare the model statistics of dust events with station data, making use of both weather code reports and visibility measurements. First, we assess the temporal variability of dust event frequency and intensity, correlating the monthly-averaged time series. We follow the classical definition of dust event frequency F_d from hourly weather code reports (Shao and Dong, 2006):

$$F_d = N_d / N_{tot}, \quad (4)$$

where N_d is the number of reported dust events, and N_{tot} is the total number of reports (including those when visibility was not reduced below 10000 m and no weather code was reported). All of the weather codes indicating the presence of dust (i.e. 06 to 09, and 30 to 35) were considered corresponding to a dust event. Based on this definition, we construct the monthly-averaged time series, so that the frequency is calculated separately for each month. To obtain the model estimate of dust event frequency, we calculate it as a fraction of time when hourly-averaged emission is above the certain threshold. We apply two constant thresholds of 1 μg m^{-2} s^{-1} and 4 μg m^{-2} s^{-1}, approximately corresponding to 70th and 85th quantiles of hourly emission rates. Taking the fraction of the time with dust emission above the threshold during the month, we obtain the model monthly time series of dust event frequency.

To analyze the intensity of individual dust events, we sample the visibility measurements for each station taking only those time steps that correspond to dust events, and calculate the monthly-averaged visibility reduction, treating it like "dust event intensity". In the case of no visibility reductions reported during the month (which is not a rare case for some stations), the 10000 m visibility value is presumed. The corresponding model time series are obtained in a way similar to that of frequency, applying the same thresholds. Dust generation intensity is considered equal to zero if there are no events above the threshold during that particular month. An approach alternative to sampling was proposed in (Mahowald et al., 2007). The authors noted the scarceness of weather code reports and proposed to filter non-aerosol (fog-driven) visibility reductions based on dew-point temperature measurements. In our case, we prefer a sampling approach as most of the station visibility reduction measurements are complemented with weather codes.

Both of the metrics described above reflect the primarily temporal, not spatial, variability of the model results. We apply the metrics to different model configurations and, as their basic effect is aimed at improving the spatial patterns, no significant differences are found. Thus some other metrics are needed to assess the reliability of dust emission spatial distributions. The technique we propose for assessing spatial patterns of dust emission is to sample the hourly visibility time series by dust

event reports, choosing the time steps when a dust event was reported, and to calculate the daily, and then 3-year mean visibility for each station. The mean emission rate is also calculated from model data sampled for the same time steps. Station data are sampled to correspond to hourly instantaneous model output: thus SPECI reports that usually take place between regular reports are not considered. We, therefore, obtain two samples of 3-year averaged station dust intensity and model emission rate (with the sample length equal to the number of stations) and calculate the correlation coefficient between them.

We calculate correlation coefficients between samples that reflect diverse highly non-linear physical phenomena. As we do not have the physical ground to assume the linear relation between these phenomena, we use Spearman's rank correlations instead of Pearson's correlations for all cases. The dust emissions and station visibility are negatively correlated, whereas the opposite is true of station dust frequency. For the sake of simplicity, here we report the emission – intensity correlations with reversed sign, keeping both coefficients positive.

2.4 MERRAero reanalysis and dust emission calibration

Very recently, a few aerosol reanalysis products have become available (Buchard et al., 2016; Inness et al., 2013). In this study, we utilize the dust emissions from MERRAero aerosol reanalysis developed by NASA (Buchard et al., 2016), which was calculated using meteorological fields from Modern-Era Retrospective Analysis for Research and Applications (MERRA I) (Rienecker et al., 2011). The reanalysis has a spatial resolution of 50 × 50 km and is available from 2003 onwards. MERRAero is built on the Goddard Earth Observing System version 5 (GEOS-5) atmospheric model, which comprises an aerosol module based on a version of the Goddard Chemistry, Aerosol, Radiation, and Transport (GOCART) model (Chin et al., 2002; Ginoux et al., 2001). GOCART simulates the interactive cycle of dust, sulfate, sea salt, black and organic carbon aerosols. MERRAero assimilates AOD observations from the MODIS sensor flying both on TERRA and AQUA satellites. The GOCART dust scheme in GEOS5 uses a topographic source function (Ginoux et al., 2001).

It is a common approach for atmospheric dust calculations to use calibration based on observations of total AOD (or assimilate AODs as in MERRAero reanalysis), as it is the basic observed quantity that characterizes an amount of aerosols in the atmosphere (Kalenderski et al., 2013; Prakash et al., 2015; Zhao et al., 2013; Zhao et al., 2010). However, in our off-line CLM4 simulations we do not calculate AOD and therefore cannot compare our results with the observed AOD directly (Shi et al., 2016). In the absence of quantitative measurements of dust generation the direct model validation is not possible (Laurent et al., 2008; Bergametti and Forêt, 2014). Therefore, we calibrate the model emissions integrated over the entire coastal area using the dust emissions from MERRAero reanalysis. We note that it is difficult to expect a global reanalysis with a relatively low spatial resolution to produce detailed spatially resolved estimates of dust emission over a narrow coastal zone. The coastal plain is only covered by one or two grid boxes (in width) by the MERRAero grid. On the other hand, the reanalysis captures the enhanced dust activity area on the western coast of the Arabian Peninsula and its integral (over the

entire coastal area) multi-year estimates of dust emission from approximately 150000 km^2 area is a reasonable reference point for model calibration. Although MERRAero dust emission has not been validated directly, the recent paper (Ridley et al., 2016) reported better seasonality of dust AOD in MERRAero compared to other datasets and pointed to potentially better dust emission patterns due to finer spatial resolution and representation of surface winds. Thus, we rely on the MERRAero estimate of 2009–2011 annual dust emission from the coastal plain (7.5 Mt) and set the T constant in (1) to produce the same dust amount in CLM4. The scaling factor depends on whether the dust emission source function is used or not. The values of scaling factors applied in our experiments are given in Table 4. We also examined the Monitoring Atmospheric Composition and Climate (MACC) reanalysis product available from ECMWF (Cuevas et al., 2015; Bellouin et al., 2013), but its spatial resolution of 80 × 80 km is coarser than that of MERRAero and it does not capture the enhanced dust emission from the coastal plain.

2.5 WRF-Chem simulations

To test the off-line CLM4 dust emission simulations we also conduct simulations with the WRF-Chem model (Grell et al., 2005). WRF-Chem includes interactive calculations of transport and chemical/microphysical transformations of trace gases and aerosols, including mineral dust and calculates dust emissions interactively. However, the WRF-Chem model is computationally demanding and at present cannot be used for multi-year fine resolution simulations in a meaningfully large spatial domain. Therefore, we compare our off-line dust generation estimates with those from two short-term WRF-Chem simulations. First, we use the results from (Kalenderski et al., 2013), who performed a 10-km run for the period of 1–20 January 2009, which included several major dust outbreaks from the Arabian Peninsula across the Red Sea. Additionally, we have performed a finer scale 4-km simulation for 1–31 January 2009, but in a smaller spatial domain focused on the Red Sea coastal plain (Fig. 1). The experiment setup is generally identical to (Kalenderski et al., 2013). The main difference is that we use a more sophisticated 8-bin Model for Simulating Aerosol Interactions and Chemistry (MOSAIC) (Zaveri et al., 2008) and photochemical Carbon Bond Mechanism (CBM-Z) (Zaveri and Peters, 1999). Another update is that instead of topographic source function (Ginoux et al., 2001) used in (Kalenderski et al., 2013), to be consistent with the current study, we use the SEVIRI source function described in section 2.2. Kalenderski et al. (2013) calibrated the dust emission calculations based on AOD observation from Solar Village AERONET station (see the previous section). As there are no AERONET stations in the smaller domain of our WRF-Chem simulation, we calibrate our model run using AODs from (Kalenderski et al., 2013) (Fig. S1).

3 Sensitivity analysis

The dust emission parameterizations calculate dust influx in the atmosphere using meteorological fields, land-surface physical properties, and, sometimes, empirical proxy information about land-surface erodibility, see Equation (1). Here we use the improved datasets of soil and vegetation physical properties and high-frequency source function as input for our dust

generation calculations. To evaluate the effect of these improved input datasets on dust generation, we use the same meteorological fields fixed in all sensitivity simulations. Firstly, we assess the sensitivity of the parameterized dust emissions to varying spatial resolution of land surface characteristics. Secondly, we apply the dust emission source function and test the results using weather station data.

3.1 Sensitivity to the horizontal resolution of surface data

Shi et al. (2016) discussed CLM4 sensitivity to the type and resolution of vegetation datasets for the entire Arabian Peninsula. They quantified the impact of high-resolution surface characteristics derived from MODIS measurements compared to the default ones on dust emission in the Arabian Peninsula. They found that dust emission is most sensitive to surface vegetation, especially in sparsely vegetated areas, which is the case for the western coastal plain. Here, we extend the sensitivity study of Shi et al. (2016) to finer scales, examining the sensitivity to the horizontal resolution of plant function type (PFT), leaf area index (LAI), stem area index (SAI), and clay mass fraction (CLY) fields. The description of those datasets is given in Table 2.

First, we consider the sensitivity of dust emissions, when changing the spatial resolution of each of the input surface characteristics separately. We perform a control experiment with all of the surface data taken at 10 × 10 km resolution (10kmALL), and four additional simulations. In the 10kmLPFT, 10kmLLAI, and 10kmLCLY experiments, we degrade the spatial resolution of one of the datasets (PFT, LAI, or CLY, respectively) in comparison with 10kmALL to 50 × 50 km. In the 50kmALL experiment, the spatial resolution of all of the above characteristics is degraded to 50 × 50 km. Wind forcing and model grid resolution of (10 km × 10 km) are kept the same for all simulations. See the definition of all relevant experiments in Table 3. Spatially uniform tuning constant $T = 0.011$ is used in all experiments (Table 4) based on 10kmALL calibration. It is important to mention that T does not affect the spatial patterns of emission, which is the primary focus of our attention in these experiments.

The differences between annual mean dust generation in 10kmALL and other simulations is depicted in Fig. 2, a–c. Overall, using high-resolution vegetation results in an appreciable increase in total dust generation with comparable contribution from PFT and LAI datasets. The changes are not strictly additive, as the emission process is non-linear, and are spatially non-uniform. Total dust emission from the coastal plain in 50kmALL is around 10 % smaller than in 10kmALL. The partial differences are smaller: 6 % (10kmLLAI) and 3 % (10kmLPFT). The spatial structure of dust generation changes with the increased resolution of vegetation datasets is spatially non-uniform. The highest differences occur along the mountain areas with substantial vegetation cover (Fig. 1a). Locally, in the central and southern parts of the coastal plain, dust generation may increase more than 50 % (Fig. 1c). In some areas south of the coastal plain, high-resolution plant function type leads to decreasing of dust emissions. The difference between the 10kmALL and 10kmLCLY simulation is not shown, as the changes are very small (less than 1 g m^{-2} a^{-1}). The likely explanation for the low model sensitivity to soil texture dataset

resolution is that its data sources may initially have been based on relatively coarse resolution observations, which have subsequently been reinterpolated to a finer grid.

To analyze the impact of fine-resolution surface data on dust generation, we perform an additional 1kmALL experiment with 1 × 1 km model grid and all the input datasets taken at the highest resolution possible (Table 2). The wind forcing is kept at 10-km resolution. The difference of annual dust emission between 1kmALL and 10kmALL simulations is shown in Fig. 2d. The results confirm the previous finding. Total dust emission further increases when switching to 1-km resolution, although the magnitude of these changes is smaller than the difference between 10kmALL and 50kmALL (Fig. 2c). Similarly, the changes are mostly associated with the vegetation and confined to the southern part of the coastal plain.

3.2 Model test with station data

In this section, we compare the model results with observations at meteorological stations, keeping in mind the limitations of this approach discussed in Sect. 2.3. To obtain the model values at station locations, we use bilinear interpolation from four surrounding grid points. If bilinear interpolation is not possible (for the coastal stations), the nearest neighbor grid point is used. First, we assess the model's ability to capture the temporal variability of dust generation in the region on monthly scales. The temporal variability of model dust emissions is mostly driven by the wind forcing. As the wind forcing is the same for all experiments, it is not surprising to find that correlation coefficients are similar in all model simulations. Therefore, we show the results for both dust event frequency (Fig. 3a) and intensity (Fig. 3b) based on 10kmALL simulation only.

For most of the stations, there are positive correlation coefficients of dust event frequency, ranging from 0.3 to 0.7 with the mean value of 0.47 ± 0.15 for 1 μg m^{-2} s^{-1} threshold and 0.52 ± 0.14 for 4 μg m^{-2} s^{-1} threshold. Most of the correlations are statistically significant at the 95 % level, suggesting reasonable model skill. For Jeddah, Bisha and Madinah, correlations become significant when a larger threshold is applied, and for Najran and Abha, only correlations with the smaller threshold are significant. The intensity correlations are not fully independent from frequency, as average visibility drop is related to the number of dust reports (in the case of severe dust storms, there are usually a number of concurrent reports that increase the frequency estimate). Despite that, we report visibility-based correlations of intensity, as these measurements are used for the spatial metrics. The results are slightly worse than for dust frequency with the mean correlation around 0.4 ± 0.2 for both thresholds, but correlations are still significant for 12 stations out of 16. Overall, the obtained correlations demonstrate a good model ability to simulate the monthly variations of dust activities.

Our correlations for most of the stations in western Saudi Arabia (Yenbo, Al Wajh, Jeddah, Makkah, Taif, Tabuk, Jizan) are higher than those between monthly satellite AOD and dust reports calculated by Yu et al. (2013). The authors reported lower correlations (0.1 – 0.3) between the monthly AOD observations and station dust reports in the west of Arabian Peninsula, compared to much higher ones in the central and eastern Peninsula (usually more than 0.4). The authors also reported a large

probability of low AOD values on dusty days for stations in the western Peninsula. Several explanations were proposed for this effect. Mentioning the instrumental shortcomings of satellite sensors over complex terrain and their low temporal resolution, Yu et al. (2013) indicated that a lot of dust is transported to the western coastal area from remote sources at higher altitudes, and therefore not captured by surface stations. On the other hand, low AOD during the days when a dust event is reported might be due to the small spatial scale of dust plumes over complex terrain. Similar mechanisms explaining low correlations between local station visibility observations and nearby AOD measurements from AERONET were also proposed in Mahowald et al. (2007).

The results obtained in the current study are consistent with those proposed by Mahowald et al. (2007) and Yu et al. (2013), supporting the proposed mechanisms. Higher correlation coefficients between station dust events and simulated emission fluxes compared to those reported by Yu et al. (2013) suggest that a large part of detected variability could be explained by local dust generation. On the other hand, Yu et al. (2013) also suggested that over the Red Sea coastal plain dust is not a predominant aerosol. This statement was questioned recently by Osipov et al. (2015) who reported, based on the CALIPSO lidar measurements during 2007–2013, that the ratio of the "not dust" to "dust" successful retrievals over this area is 2.04 %.

To assess the spatial distribution of simulated dust emissions and choose the best model settings, we use the metrics described in Sect. 2.3. The model and station data are sampled to include the visibility reductions during dust reports only. The number of reported dust events per station during the 3 years considered in the study ranges from less than 100 at two stations (72 dust reports in Makkah and 64 dust reports Al Wajh) to up to 400. Given this, the two stations with the lowest numbers of observations are excluded from the final spatial analysis. The Al Wajh station is situated just several hundred meters away from the sea shore, and the low number of dust reports may be due to small-scale circulation features. Model and satellite dataset resolution may be not enough to represent the local circulation, surface characteristics and emission rate with the desired accuracy. As for the Makkah station, the low number of dust reports may be caused by instrumentation errors and insufficient quality control; the station is not collocated with the airport and the data are not used in aviation services.

The spatial correlations with station samples are calculated for three basic simulations (50kmALL, 10kmALL and 1kmALL) with and without the statistical source function (Fig. 3c). The results show that using the SEVIRI source function significantly improves the spatial structure of dust emission. Even our short-sample statistics allow high correlations to be obtained for all of the three basic simulations. Increasing the surface datasets' resolution, together with applying the source function, leads to increasing the correlation coefficient to 0.68, 0.77 and 0.85 depending on the basic simulation. The correlation coefficients for simulations without source functions are not statistically significant. The 50kmALL correlation is almost zero, whereas correlations in 10kmALL and 1kmALL experiments are almost equal. This result is expected, implying high-resolution datasets only add small-scale details that are difficult to capture with a coarse observational network.

Along with the SEVIRI source function, we use several others (see Sect. 2.2). However, topographic, geomorphic and MODIS-based source functions are all unable to significantly increase the model skill. For topographic and geomorphic source functions this can be explained by the fact that they were developed for large-scale models initially, thus, they are not expected to work well on regional scales. The MODIS source function, on the other hand, is based on measurements from a polar-orbiting satellite that has low temporal resolution (only two measurements per day), insufficient to capture the local dust phenomena caused primarily by circulations with a prominent diurnal cycle (Ginoux and Torres, 2003; Kocha et al., 2013; Yu et al., 2013) (see Sect. 4.3).

4 Dust emission multi-year estimate

The above analysis shows that 50kmALL, 10kmALL and 1kmALL model configurations with the source function based on high-frequency satellite measurements provide quite realistic results (spatial correlation with respect to observations of 0.68, 0.77 and 0.85). 1kmALL simulation with the SEVIRI source function has the highest resolution and correlation coefficient; therefore, we use it for further analysis of dust emission climatology and discuss the major dust source areas within the coastal plain, diurnal and seasonal cycles of emission from those areas, as well as their annual mean and variability.

4.1 Emissions from the main dust sources

We first address the spatial distribution of dust generating areas (hot spots), and then turn to the temporal variability. To examine the dust generation regime, we discuss the three-year averaged (2009–2011) spatial patterns of total generated dust amount (Fig. 4), dust emission frequency, intensity and maximum emission rate (Fig. 5). Dust emission hot spots are defined as areas where generated dust amount and emission frequency are two times higher, and dust event intensity is 1.5 times higher than domain-averaged values. The locations of hot spots are shown by shaded areas on a real color satellite image (Fig. 4c).

To analyze the mechanisms initiating dust generation, we examine the wind forcing and its variability (Fig. 6). We pay special attention to dust generation mechanisms in the hot spot areas. Although the period of three years is quite short to be considered as climatologically representative, it is shown below that dust generation in this area generally, has low interannual variability. In the current and subsequent sections, we use the same threshold for frequency and intensity ($4\ \mu g\ m^{-2}\ s^{-1}$) as for calculation of correlation coefficients with observations.

The total dust emission is spatially variable, changing from zero to more than 100 g m^{-2} a^{-1} in some areas (Fig. 4a). Figure 4a and Fig. 5a–b depict a similar pattern, suggesting that the areas with the largest and most frequent dust outbreaks coincide. The dust emission hot spots occupy around 8 % of the total coastal area (Fig. 4c). The zones where the maximum emission rate occurs (Fig. 5c) comply well with the hot spots. Most of the hotspots correspond to lowlands. The hotspots are

located not directly near the coastal areas, but rather near the western hillsides of the Hejaz Mountains, in the dry riverbeds ("wadis") where alluvial deposits are available. The primary hot spot zone in the northern part of the study area (SM1, Fig. 5c) spans along the coast between the cities of Yenbo and Umluj. Emission intensity reaches its maximum value here (over 12 μg m^{-2} s^{-1}), and emission frequency is over 0.25. As seen from Fig. 6d, this hot spot is mostly driven by high winds. Dust event frequency is highly variable here, which is explained by the wind forcing variability (Fig. 6e). Dust generation and wind forcing peak in Spring. These hot spot conditions are prevalent in this part of the coastal plain.

The chain of dust hot spots in the southern part of the coastal plain stretches from Makkah to Abha. Three isolated hot spot zones can be identified. The first one lies to the south of Makkah and Taif (SM2, Fig. 5c). The second zone is in the proximity of Al Bahah (SM3). A third small but intensive zone is located on a coast near the city of Al Qunfudhah (SM4). The frequency of dust events is around 0.25 in these southern hot spot areas, and emission intensity reaches more than 10 μg m^{-2} s^{-1}.

The SM2 hot spot is driven by moderate winds with considerable intermonth variability, thus the frequency of dust activity changes during the year, having its peak in Summer months. In the rest of the southern hot spots (SM3 and SM4, Fig. 5c), wind activity is weak (Fig. 6d) and dust emission is mainly facilitated by the low erosion threshold and is increased due to source function correction. The intermonth variability of dust emission is relatively low here and is predominantly driven by dust frequency variations. There are two other smaller, isolated emission zones: a hot spot near the Gulf of Aqaba in the north (SM6, Fig. 5c) and an intensive hot spot area in the south near Jizan (SM5, Fig. 5c).

Dust emission in the large area between 21° N and 24° N is relatively uniform and reaches quite a considerable volume. Although there are no major hot spots, this area contributes significantly to the total dust generation, producing around 2 Mt of dust per year. The annual-mean dust frequency is around 0.15 here, and the average dust intensity is 7–9 μg m^{-2} s^{-1}, with both of them reaching maximum in Winter. Dust generation shows high intermonth variability, but in contrast to SM1, the variability is mostly caused by variations in dust emission intensity. Examining the wind circulation in this area, we find that the high variability of dust event intensity is caused by high monthly mean values in Winter and early Spring. Dust intensity averaged over this part of the coastal plain reaches 36 μg m^{-2} s^{-1} during a January 2009 dust storm and 28 μg m^{-2} s^{-1} during March 2011. High maximum values of dust intensity are also seen in Fig. 5c. On the other hand, the intermonth variability of dust frequency is relatively low here. Dust outbreaks are driven by short-lived wind gusts, likely to be explained by diurnally varying jet winds (Gille and Llewellyn Smith, 2014; Jiang et al., 2009). This is confirmed by analyzing the sub-month variability of winds (not shown). During January 2009 and March 2011, hourly wind speed variability was two times higher than average, although mean wind speed was only 20 % higher than the annual average. Due to the non-linear character of dust generation, these wind gusts may lead to high monthly values of dust generation intensity. Similar processes also occur in the north of the SM1 hot spot.

To further confirm this idea we analyze the WRF-Chem simulations discussed in section 2.5. The jets that originate in the coastal plain and bring dust over the Red Sea are both observed by satellites and simulated in the models (Fig. S1). The spatial patterns of dust generations in WRF-Chem and CLM4 simulations are consistent (Fig. S2). However, the magnitude of dust emission in the models varies. In the 20-days simulation by Kalenderski et al. (2013), 1.39 Mt of dust is generated compared to 0.66 Mt in CLM4. In the WRF-Chem–MOSAIC run performed in the current study 1.5 Mt of dust is produced during January 2009 compared to 0.92 Mt in CLM4. Thus, the daily average dust generation from the coastal plain in WRF-Chem is 40–50% larger than in CLM4 which is in the range of expected uncertainty between off-line and coupled dust simulations.

The annual mean spatial distribution of dust emission in MERRAero for the period of 2003–2015 is depicted in Fig. 4b. Due to its coarse resolution, MERRAero hardly resolves the local-scale emission areas. Nevertheless, the dust generation pattern reasonably complies with the results obtained with the high-resolution model and features the primary emission zones. Two major emission zones in Fig. 4b can be identified as SM1 and SM2, although SM1 is smaller than in our results and its peak generation is further to the north. The SM2 source area is the strongest, covering large neighboring territories. MERRAero generates some dust in the area of SM3 and SM4 hot spots, although the amount is less than in CLM4. The emission zone near Jizan (SM5) is also present in the reanalysis. Overall, the dust emission patterns from CLM4 and independent reanalysis are quite consistent. Below we show that CLM4 dust emission seasonal cycles are consistent with reanalysis as well.

4.2. Temporal variability of dust emissions

4.2.1 Seasonal cycle of dust emissions

The seasonal and interannual variability of dust storms in the Arabian Peninsula has been extensively discussed in recent studies (Alobaidi et al., 2016; Notaro et al., 2013; Notaro et al., 2015; Rezazadeh et al., 2013; Shalaby et al., 2015; Yu et al., 2013; Yu et al., 2015). Most of the studies report the period of maximum dust activity is from February until July–August, but the peak month varies depending on location and data source (Notaro et al., 2013; Shalaby et al., 2015; Yu et al., 2013). In the north of the Arabian Peninsula, late Winter – early Spring peak is more common, and in the south – southeast desert regions dust activity tends to reach its maximum in Summer. According to Notaro et al. (2013) and references therein, the late Winter – early Spring dust peak in the north-west is due to the cold fronts associated with cyclones from the Mediterranean, whereas the Summer peak in the south is due to diurnal heating, turbulent mixing, and strong Summer Shamal winds (Yu et al., 2015). In this study, we find the seasonality of dust emission from local sources to be quite consistent with previously reported results.

The seasonal cycles (averaged over three years) of total dust generation, monthly mean dust frequency, intensity and monthly maximum emission rate are shown in Fig. 7. The analysis is conducted over the entire coastal domain and separately for the northern and southern parts (separated at 21° N) of the coastal plain and hot spot areas. To compare our

model results with reanalysis, the corresponding values from MERRAero averaged over 2003–2015 are also plotted together with standard deviation intervals.

The total emission flux (Fig. 7a) exhibits a pronounced seasonal cycle with a dual maximum in March and July and minimum in February and October. The peaks originate from a distinct character of seasonal cycles in the northern and southern parts of the coastal plain. The March peak is only evident in the northern area and is mostly caused by increased intensity during the dust storm episodes (Fig. 7c). High intensity is also seen in January in the north, partially caused by a dust storm in 2009. The peak Winter and Spring seasons for dust intensity in the north are also shown in Fig. 5b. Conversely, the July peak is due to both frequency (Fig. 5a, Fig. 7b) and intensity (Fig. 5b, Fig. 7c) reaching its maximums in the southern part of the coastal plain, although they are lower than that in the northern coastal plain. The seasonal cycle of maximum dust emission rate (Fig. 7d) generally follows that of intensity. Overall, we can conclude that the different climate and surface conditions in the north and south of 21˚N drive the spatial variations of the seasonal cycle of dust emission.

The seasonal cycle of dust emissions from the hot spots is consistent with the seasonal variability of the total dust generation from the coastal plain. Since the hot spots are in both the northern and southern parts of the coastal plain, the seasonal cycles of total emissions are smoother than for the northern and southern coastal plain separately. In the hot spots, magnitudes of dust frequency, intensity, and maximum emission rate are 2–2.5 times higher than that for the total coastal area and are above the mean plus standard deviation threshold in MERRAero. The overall amount of dust emitted from the hot spot areas is 1.9 Mt a^{-1} or 25 % of the total emissions, while hot spots occupy only 12800 km^2 or less than 10 % of the total area. This fact indicates that the soil mineralogical composition and wind variability have to first be studied in these hot spot areas (Prakash et al., 2016).

The seasonal cycles of dust emissions in MERRAero and CLM4 show similar behavior. As CLM4 dust emissions are scaled to match MERRAero, we only compare the seasonal variations, not averages. In general, seasonal cycles are in good agreement. Summer dust emissions are the largest in MERRAero, similar to CLM4 results in the southern part of the coastal plain. The Spring peak is not present in the reanalysis. One of the possible reasons is the coarse resolution of reanalysis that does not capture the local-scale wind patterns that cause the Spring peak. Similarly, Yu et al. (2013) reported that satellite AOD measurements in the western Arabian Peninsula do not feature the early Spring peak (as opposed to station dust records), attributing it to the local character of springtime dust generation.

With the exception of the March peak, the seasonal cycle of CLM4 dust generation lies within the MERRAero standard deviation interval. This is also true for dust event frequency and intensity, although the frequency is slightly smaller than in reanalysis and intensity is slightly larger. It may be caused by the fact that, in the case of MERRAero, these quantities were calculated with the same threshold, but based on three-hourly data; therefore, some dust outbreaks on the threshold

borderline are missed. As expected, maximum dust emission rates in CLM4 are larger than in reanalysis, being substantially above the standard deviation interval, especially in March and July.

The total annual dust emission from the entire 147000 km^2 coastal area is 7.5 Mt as in MERRAero reanalysis. This dust influx in the atmosphere is substantial, and assuming that a significant portion of this dust could be transported to the Red Sea, might cause dust deposition to the Red Sea comparable to that of 6 Mt a^{-1} from the major dust storms (Prakash et al., 2015). About 4.9 Mt a^{-1}, or 65 % of the total emission is generated from the northern part of the coastal plain. Analyzing dust emission in MERRAero for the entire 2003 – 2015 period we find it varies only slightly 7.5 ± 0.5 Mt a^{-1}. Small inter-annual variability of emissions and a permanent distribution of the dust hot spots (Fig. 6 a-c, Fig. 7) suggest that the coastal plain is a stable dust source.

4.2.2 Diurnal cycle of dust emissions

The annual average diurnal cycles of total dust generation, frequency, intensity and maximum emission rate are computed from the 3-year simulations (Fig. 8 a–d). Total dust generation, frequency, and maximum emission rate have a pronounced diurnal cycle, consistent with wind speed intensifying during solar peak. Both total dust emission and frequency peak around early afternoon, at 12:00–14:00 UTC, with a slight shift between the northern and southern parts of the coastal plain due to the latitudinal extent. The frequency of dust events during the daily maximum is around 0.35 both in the north and in the south. Overall, around 80 % of airborne dust is generated between 07:00–16.00 UTC. The nighttime dust emission in the northern part is much stronger due to the larger number of cold fronts passing through the northern Red Sea (Notaro et al., 2013; Yu et al., 2015). In the south, the frequency of nighttime dust events is lower due to the different character of wind forcing with a more pronounced diurnal cycle (Notaro et al., 2013). The frequency of dust events in the hotspot areas during the peak hours reaches 0.8, but during the nighttime, it is less than 0.05.

Dust emission intensity has a different diurnal cycle. In the north, the daytime maximum of dust frequency corresponds to minimum intensity. The total distribution of dust events above the threshold during these hours is characterized by a large number of moderate-intensity events, thus, the average emission is relatively small. On the other hand, the small total number of dust events above the threshold in the nighttime leads to a larger contribution from strong events and increased average intensity. The diurnal range of emissions in the northern coastal plain is from 7 to 12 μg m^{-2} s^{-1}. In the southern part, the nighttime intensity is smaller due to the presence of areas with zero contribution to the average intensity, as there are no dust events exceeding the threshold intensity. This results in an almost uniform diurnal intensity cycle in the southern part of the coastal plain (5–7 μg m^{-2} s^{-1}). In the hot spot areas, average dust intensity has two diurnal peaks at 13.00 and 22.00, and reaches the minimum at 17.00 UTC.

The diurnal cycle of dust maximum emission rate is also different in the north and south. It peaks at 9:00 UTC in the northern areas with a diurnal range of 20–50 μg m^{-2} s^{-1}, and at 14:00 UTC in the south with a diurnal range of 15–35 μg m^{-2}

s^{-1}. Maximum emission rate averaged over the coastal plain follows the one in the north, but the peak value is smaller (40 μg m^{-2} s^{-1}). In the hot spot areas, the diurnal cycle of maximum emission rate is even more pronounced. Daily maximum emission peaks during 9:00–15:00 UTC and reaches 100 μg m^{-2} s^{-1}. It is still significant during the nighttime, reaching more than 50 μg m^{-2} s^{-1}. High nighttime values of dust emission intensity and maximum emission rate in the hot spot areas despite low event frequency indicate that the rare, severe nighttime dust generation is much more pronounced in the hot spots compared to other areas of the coastal plain.

4.3 Mineralogical composition

Dust elemental composition has a variety of physical and biogeochemical impacts. Perlwitz et al. (2015), Scanza et al. (2015), and Zhang et al. (2015) have applied sophisticated modeling tools to study the dust mineral composition on global scales. In our case, we concentrate on a fine-scale narrow coastal area, as generated dust has the potential to deposit directly to the sea. Thus, we aim at estimating the amount of minerals generated from the coastal plain and assume it is representative of the mineral composition of dust deposited to the Red Sea. To calculate the emitted mineral fluxes we use the global datasets of dust mineral composition, GMINER30, and soil texture, SOILPOP30, developed by Nickovic et al. (2012). SOILPOP30 provides the global coverage of fractions for three soil texture classes (clay, silt, and sand). GMINER30 provides the soil type and corresponding mineral composition. We assume that the relative proportions of minerals in the airborne dust are the same as those of the parent soils. The largest size bin of emitted dust (transport bin) in CLM4 is 5–10 μm, whereas the silt fraction in GMINER30 corresponds to 2–50 μm. This allows us to assume following Nickovic et al. (2013) that emitted dust is a mixture of clay and silt particles only (without coarser fractions). Thus, emitted mineral fractions are weighted with the clay and silt content in the soil. For minerals that are present in both clay and silt, the weighted values are summed.

Our assumption that the mineral composition of emitted dust is the same as that of parent soil is reasonable for clay soil fraction (Caquineau et al., 1998; Lafon et al., 2004), but it does not always hold in general case (Claquin et al., 1999; Perlwitz et al., 2015). During the airborne dust life cycle, both chemical (dust aging) and physical fractionation processes occur and change the dust mineral composition and size distribution. However, due to the short pathway from the coastal plain to the sea, dust composition changes due to gravitational settling and chemical transformations become less important for local dust particles compared to those subjected to long-range transport. Another issue is the instrumental bias of GMINER30 dataset that was produced using the wet sieving technique. This technique strongly disperses soil aggregates (Shao, 2001; Laurent et al., 2008; Perlwitz et al., 2015), adding uncertainty to the partitioning of minerals between clay and silt fractions. As long as of our primary interest are the iron oxides and phosphorus that limit the marine productivity, the instrumental bias is less important in our case.. Nickovic et al. (2012) assume the same fraction of phosphorus and nearly the same of iron oxides in clay and silt. Having said this, our assessment may serve as an initial rough estimate of the mineral composition of dust deposited in the sea from local sources.

The minerals' annual emissions are calculated using dust emission flux obtained with the 1kmALL simulation and the SEVIRI source function applied. Figure 9 shows annual amounts of minerals emitted from the coastal plain. Quartz is the most abundant mineral, comprising around 40 % of the total emission. 25 % of the total emission corresponds to feldspars, followed by illite, smectite, kaolinite, calcite, gypsum, hematite and goethite (the iron source), and phosphorus. The Arabian Red Sea coast provides 76±5 Kt of iron oxides and 6±0.4 Kt of phosphorus annually. Over 60 % of iron oxides and phosphorus are emitted from the northern part of the coastal plain, acting as a nutrition source for the oligotrophic northern part of the Red Sea. Although only a portion of dust emitted from the Arabian coast is deposited to the Red Sea, due to the close proximity of the dust generation area to the sea (especially in the northern coastal plain) and the structure of mesoscale circulation that includes jets and breezes, its role in total mineral deposition to the Red Sea could be significant.

5 Conclusions

This study focused on the dust emission from the Red Sea Arabian coastal plain. We applied the off-line CLM4 land surface model to perform high-resolution simulations of dust emission for 2009–2011 using up-to-date land surface datasets. The magnitude of integrated over the entire area dust emissions was tuned to fit the estimate from MERRAero reanalysis, while the spatial structure was calculated within CLM4, forced by 10 × 10 km resolution meteorology from WRF simulations. To test the simulated dust emission, we developed the corresponding metrics and performed a comparison with the weather station reports of horizontal visibility and present weather code. We obtained significant correlations for monthly time series of dust event frequency and intensity (station-mean correlation coefficients of 0.5 and 0.4), indicating reasonable model performance. The results confirmed that dust emission from local sources on the Arabian Red Sea coastal plain is significant and supported the hypothesis by Yu et al. (2013) that the dust activity in this area may be caused by local-scale dust outbreaks.

Within the proposed framework, we performed a sensitivity study and demonstrated that high-resolution input surface datasets might add fine-scale details to dust generation patterns. The spatial resolution of vegetation datasets was shown to alter total dust emissions by up to 10 %. We confirmed the findings by Shi et al. (2016), showing that the increased resolution of the vegetation dataset leads to significant dust flux in some zones where it was very weak when coarse input data fields were used. We estimated the comparable contribution to total dust emission from the increased resolution of the plant function type dataset on one hand and the leaf area index and stem area index on the other hand.

To improve the spatial structure of dust generation, we calculated and applied a statistical source function based on the high-frequency geostationary measurements from the SEVIRI instrument. We showed that this approach allows a better representation of dust sources. Depending on model resolution, the statistically significant model skill (spatial correlation coefficient based on comparison with 14 ground stations) varied from 0.68 to 0.85. Without the source function, the spatial model skill was not statistically significant.

Following the evaluation tests, we based our estimates on model simulation with 1 × 1 km spatial resolution and SEVIRI source function. The estimate of total dust emission from the coastal plain, tuned to fit emissions in the MERRAero reanalysis, is 7.5±0.5 Mt a^{-1} (approximately 50 g m^{-2} a^{-1}). Over 65 % of dust is generated in the northern part of the coastal plain. The seasonality of dust emission differs substantially in the northern and southern parts of the coastal plain. In the south, the annual maximum of dust emission occurs in July, whereas in the north March is the peak month of dust activity. This distinct character is due to the contrasting forcing mechanisms: in the north, emission is caused by strong, diurnally variable, cold season winds, whereas in the south it is largely controlled by a low erodibility threshold and soil moisture. These features result in dual maximum values within the seasonal cycle of total dust emission from the coastal area in March and July.

The spatial pattern of total annual dust emission is highly non-uniform, reaching more than 100 g m^{-2} a^{-1} in some hot spot areas. The chain of hot spots stretches alongside the coastal zone, with most of them located in the lowlands near the western hillsides of the Hejaz Mountains – riverbeds that are usually considered the source of alluvial material. The hot spots occupy around 8 % of the coastal area and generate over 25 % (1.9 Mt a^{-1}) of total dust. The emission pattern is in reasonable agreement with the coarse-resolution results from the MERRAero global reanalysis, despite the fact that the reanalysis dust model uses a different source function. We also showed that dust generation has a pronounced diurnal cycle. Around 80 % of dust is generated during the daytime, between 07:00–16.00 UTC, with dust emission rate and emission frequency peaks during early afternoon (12:00–14:00 UTC).

The total dust generation from the coastal plain of 7.5±0.5 Mt a^{-1} is comparable to the estimate of annual dust deposition to the Red Sea of 6 Mt a^{-1} due to major dust storms (Prakash et al., 2015). Small inter-annual variability indicates that the study area is a stable dust source. The comparison with the short-term WRF-Chem simulations suggests that this estimate could be even larger, as WRF-Chem produces 40–50 % more dust, supporting the finding that the coastal plain is a significant dust source. Our calculations of the dust mineralogy suggest that 76±5 Kt of iron oxides and 6±0.4 Kt of phosphorus are emitted from the coastal plain annually.

Author contributions

Anatolii Anisimov performed the data processing, developed the technique for comparison with observations, conducted the comparison with reanalysis, performed the WRF-Chem simulation, formulated the results and wrote the final paper.
Weichun Tao designed the experiments, ran the model simulations, calculated the source functions, performed the basic analysis and wrote the paper draft.
Georgiy Stenchikov formulated the problem, directed the research, and edited the paper.
Stoitchko Kalenderski ran the WRF model to obtain the meteorological forcing for the dust emission calculations.
P. Jish Prakash and Weichun Tao worked together on the dust mineral analysis.

Zong-Liang Yang, one of the developers of CLM4, helped in setting the CLM4 runs.
Mingjie Shi and Weichun Tao worked together on collecting the land surface data.

Acknowledgements

We thank Prof. V. Ramaswamy and Dr. Paul A. Ginoux of GFDL for valuable discussions. We also thank Prof. Johann Engelbrecht and Ms. Linda Everett for proofreading the article. The research reported in this publication was supported by the King Abdullah University of Science and Technology (KAUST). For computer time, this research used the resources of the Supercomputing Laboratory at KAUST in Thuwal, Saudi Arabia.

References

Acker, J., Leptoukh, G., Shen, S., Zhu, T. and Kempler, S.: Remotely-sensed chlorophyll a observations of the northern Red Sea indicate seasonal variability and influence of coastal reefs, J. Mar. Syst., 69, 191–204, doi:10.1016/j.jmarsys.2005.12.006, 2008.

Ackerman, S. A. and Cox, S. K.: Surface weather observations of atmospheric dust over the southwest summer monsoon region, Meteorol. Atmos. Phys., 41, 19–34, doi:10.1007/BF01032587, 1989.

Alobaidi, M., Almazroui, M., Mashat, A. and Jones, P. D.: Arabian Peninsula wet season dust storm distribution: regionalization and trends analysis (1983-2013), Int. J. Climatol., doi:10.1002/joc.4782, 2016.

Baker, A. R. and Croot, P. L.: Atmospheric and marine controls on aerosol iron solubility in seawater, Mar. Chem., 120, 4–13, doi:10.1016/j.marchem.2008.09.003, 2010.

Banks, J. R., and Brindley, H. E.: Evaluation of MSG-SEVIRI mineral dust retrieval products over North Africa and the Middle East, Rem. Sens. Environ., 128, 58–73, doi:10.1016/j.rse.2012.07.017, 2013.

Banks, J. R., Brindley, H. E., Flamant, C., Garay, M. J., Hsu, N. C., Kalashnikova, O. V, Klüser, L. and Sayer, A. M.: Intercomparison of satellite dust retrieval products over the west African Sahara during the Fennec campaign in June 2011, Remote Sens. Environ., 136, 99–116, doi:http://dx.doi.org/10.1016/j.rse.2013.05.003, 2013.

Barkan, J., Kutiel, H., and Alpert, P.: Climatology of dust sources in North Africa and the Arabian peninsula, based on TOMS data, Indoor Built Environ., 13, 407–419, doi:10.1177/1420326x04046935, 2004.

Bellouin, N., Quaas, J., Morcrette, J. J., and Boucher, O.: Estimates of aerosol radiative forcing from the MACC re-analysis, Atmos. Chem. Phys., 13, 2045–2062, doi:10.5194/acp-13-2045-2013, 2013.

Bergametti, G. and Forêt, G.: Dust deposition, in Mineral dust: A key player in the Earth system, edited by P. Knippertz and J.-B. W. Stuut, pp. 179–200, Springer Netherlands, Dordrecht., 2014.

Brindley, H. E. and Russell, J. E.: An assessment of Saharan dust loading and the corresponding cloud-free longwave direct radiative effect from geostationary satellite observations, J. Geophys. Res., 114, D23201, doi:10.1029/2008JD011635, 2009.

Buchard, V., da Silva, A. M., Randles, C. A., Colarco, P., Ferrare, R., Hair, J., Hostetler, C., Tackett, J. and Winker, D.: Evaluation of the surface PM2.5 in Version 1 of the NASA MERRA Aerosol Reanalysis over the United States, Atmos. Environ., 125, 100–111, doi:10.1016/j.atmosenv.2015.11.004, 2016.

Bullard, J. E., Harrison, S. P., Baddock, M. C., Drake, N., Gill, T. E., McTainsh, G. and Sun, Y.: Preferential dust sources: A geomorphological classification designed for use in global dust-cycle models, J. Geophys. Res., 116, F04034, doi:10.1029/2011JF002061, 2011.

Camino, C., Cuevas, E., Basart, S., Alonso-Pérez, S., Baldasano, J. M., Terradellas, E., Marticorena, B., Rodríguez, S. and Berjón, A.: An empirical equation to estimate mineral dust concentrations from visibility observations in Northern Africa, Aeolian Res., 16, 55–68, doi:10.1016/j.aeolia.2014.11.002, 2015.

Caquineau, S., Gaudichet, A., Gomes, L., Magonthier, M.-C. M. and Chatenet, B.: Saharan dust: Clay ratio as a relevant tracer to assess the origin of soil-derived aerosols, Geophys. Res. Lett., 25, 983–986, doi:10.1029/98GL00569, 1998.

Chase, Z., Paytan, A., Beck, A., Biller, D., Bruland, K., Measures, C., and Sañudo-Wilhelmy, S.: Evaluating the impact of atmospheric deposition on dissolved trace-metals in the Gulf of Aqaba, Red Sea, Mar. Chem., 126, 256–268, doi:10.1016/j.marchem.2011.06.005, 2011.

Chin, M., Ginoux, P., Kinne, S., Torres, O., Holben, B. N., Duncan, B. N., Martin, R. V., Logan, J. a., Higurashi, A. and Nakajima, T.: Tropospheric Aerosol Optical Thickness from the GOCART Model and Comparisons with Satellite and Sun Photometer Measurements, J. Atmos. Sci., 59, 461–483, doi:10.1175/1520-0469(2002)059<0461:TAOTFT>2.0.CO;2, 2002.

Choobari, O. A., Zawar-Reza, P. and Sturman, A.: The global distribution of mineral dust and its impacts on the climate system: A review, Atmos. Res., 138, 152–165, doi:10.1016/j.atmosres.2013.11.007, 2014.

Chou, M.-D. and Suarez, M. J.: A solar radiation parameterization for atmospheric studies, Technical Report Series on Global Modeling and Data Assimilation, NASA Tech. Memo., 104606, 15, 40 pp., 1999.

Claquin, T., Schulz, M., and Balkanski, Y. J.: Modeling the mineralogy of atmospheric dust sources, J. Geophys. Res.-Atmos., 104, 22243–22256, doi:10.1029/1999JD900416, 1999.

Cowie, S. M., Knippertz, P., and Marsham, J. H.: A climatology of dust emission events from northern Africa using long-term surface observations, Atmos. Chem. Phys., 14, 8579–8597, doi:10.5194/acp-14-8579-2014, 2014.

Cuevas, E., Camino, C., Benedetti, A., Basart, S., Terradellas, E., Baldasano, J. M., Morcrette, J. J., Marticorena, B., Goloub, P., Mortier, A., Berjón, A., Hernández, Y., Gil-Ojeda, M., and Schulz, M.: The MACC-II 2007–2008 reanalysis: atmospheric dust evaluation and characterization over northern Africa and the Middle East, Atmos. Chem. Phys., 15, 3991–4024, doi:10.5194/acp-15-3991-2015, 2015.

Davis, S. R., Pratt, L. J., and Jiang, H.: The Tokar Gap jet: Regional circulation, diurnal variability, and moisture transport based on numerical simulations, J. Clim., 28, 5885–5907, doi:10.1175/JCLI-D-14-00635.1, 2015.

Edgell, H. S.: Arabian Deserts. Nature, Origin and Evolution, Springer, Dordrecht, Netherlands, 592 pp., 2006.

Engelstaedter, S., Tegen, I. and Washington, R.: North African dust emissions and transport, Earth-Science Rev., 79, 73–100, doi:10.1016/j.earscirev.2006.06.004, 2006.

Evan, A. T., Fiedler, S., Zhao, C., Menut, L., Schepanski, K., Flamant, C., and Doherty, O.: Derivation of an observation-based map of North African dust emission, Aeolian Res., 16, 153–162, doi:10.1016/j.aeolia.2015.01.001, 2015.

Furman, H. K. H.: Dust storms in the Middle East: sources of origin and their temporal characteristics, Indoor Built Environ., 12, 419–426, doi:10.1177/1420326X03037110, 2003.

Gille, S. T., and Llewellyn Smith, S. G.: When land breezes collide: Converging diurnal winds over small bodies of water, Q J. Roy. Meteor. Soc., 140, 2573–2581, doi:10.1002/qj.2322, 2014.

Ginoux, P., Chin, M., Tegen, I., Prospero, J. M., Holben, B., Dubovik, O. and Lin, S.-J.: Sources and distributions of dust aerosols simulated with the GOCART model, J. Geophys. Res.-Atmos., 106, 20255–20273, doi:10.1029/2000JD000053, 2001.

Ginoux, P. and Torres, O.: Empirical TOMS index for dust aerosol: Applications to model validation and source characterization, J. Geophys. Res., 108, 4534, doi:10.1029/2003JD003470, 2003.

Ginoux, P., Garbuzov, D. and Hsu, N. C.: Identification of anthropogenic and natural dust sources using Moderate Resolution Imaging Spectroradiometer (MODIS) Deep Blue level 2 data, J. Geophys. Res., 115, D05204, doi:10.1029/2009JD012398, 2010.

Ginoux, P., Prospero, J. M., Gill, T. E., Hsu, N. C., and Zhao, M.: Global-scale attribution of anthropogenic and natural dust sources and their emission rates based on MODIS deep blue aerosol products, Rev. Geophys., 50, 1–36, doi:10.1029/2012RG000388, 2012.

Goudie, A. S., and Middleton, N.J.: Desert dust in the global system, Springer, 287 pp., 2006.

Grell, G., Peckham, S. E., Schmitz, R., A., M. S., Frost, G., Skamarock, W. C., and Eder, B.: Fully coupled "online" chemistry within the WRF Model, Atmos. Environ., 39, 6957–6975, 2005.

Hamidi, M., Kavianpour, M., and Shao, Y.: Synoptic analysis of dust storms in the Middle East, Asia-Pacific J Atmos Sci, 49, 279–286, doi:10.1007/s13143-013-0027-9, 2013.

Hamidi, M., Kavianpour, M. R., and Shao, Y.: Numerical simulation of dust events in the Middle East, Aeolian Res., 13, 59–70, doi:10.1016/j.aeolia.2014.02.002, 2014.

Hong, S.-Y., Noh, Y. and Dudhia, J.: A new vertical diffusion package with an explicit treatment of entrainment processes, Mon. Weather Rev., 134, 2318–2341, doi:10.1175/MWR3199.1, 2006.

Huneeus, N., Schulz, M., Balkanski, Y., Griesfeller, J., Prospero, J., Kinne, S., Bauer, S., Boucher, O., Chin, M., Dentener, F., Diehl, T., Easter, R., Fillmore, D., Ghan, S., Ginoux, P., Grini, A., Horowitz, L., Koch, D., Krol, M. C., Landing, W., Liu, X., Mahowald, N., Miller, R., Morcrette, J. J., Myhre, G., Penner, J., Perlwitz, J., Stier, P., Takemura, T., and Zender, C. S.: Global dust model intercomparison in AeroCom phase I, Atmos. Chem. Phys., 11, 7781–7816, doi:10.5194/acp-11-7781-2011, 2011.

Hurrell, J. W., Holland, M. M., Gent, P. R., Ghan, S., Kay, J. E., Kushner, P. J., Lamarque, J.-F., Large, W. G., Lawrence, D., Lindsay, K., Lipscomb, W. H., Long, M. C., Mahowald, N., Marsh, D. R., Neale, R. B., Rasch, P., Vavrus, S., Vertenstein, M., Bader, D., Collins, W. D., Hack, J. J., Kiehl, J., and Marshall, S.: The Community Earth System Model: A framework for collaborative research, B. Am. Meteorol. Soc., 94, 1339–1360, doi:10.1175/BAMS-D-12-00121.1, 2013.

Inness, A., Baier, F., Benedetti, A., Bouarar, I., Chabrillat, S., Clark, H., Clerbaux, C., Coheur, P., Engelen, R. J., Errera, Q., Flemming, J., George, M., Granier, C., Hadji-Lazaro, J., Huijnen, V., Hurtmans, D., Jones, L., Kaiser, J. W., Kapsomenakis, J., Lefever, K., Leitão, J., Razinger, M., Richter, A., Schultz, M. G., Simmons, A. J., Suttie, M., Stein, O., Thépaut, J. N., Thouret, V., Vrekoussis, M., Zerefos, C., and the MACC team: The MACC reanalysis: an 8 yr data set of atmospheric composition, Atmos. Chem. Phys., 13, 4073–4109, doi:10.5194/acp-13-4073-2013, 2013.

Janjić, Z. I.: The step-mountain Eta Coordinate Model: Further developments of the convection, viscous sublayer, and turbulence closure schemes, Mon. Weather Rev., 122, 927–945, doi:10.1175/1520-0493(1994)122<0927:TSMECM>2.0.CO;2, 1994.

Jiang, H., Farrar, J. T., Beardsley, R. C., Chen, R. and Chen, C.: Zonal surface wind jets across the Red Sea due to mountain gap forcing along both sides of the Red Sea, Geophys. Res. Lett., 36, L19605, doi:10.1029/2009GL040008, 2009.

Jickells, T. D., An, Z. S., Andersen, K. K., Baker, A. R., Bergametti, G., Brooks, N., Cao, J. J., Boyd, P. W., Duce, R. A., Hunter, K. A., Kawahata, H., Kubilay, N., laRoche, J., Liss, P. S., Mahowald, N., Prospero, J. M., Ridgwell, A. J., Tegen, I., and Torres, R.: Global iron connections between desert dust, ocean biogeochemistry, and climate, Science, 308, 67–71, 2005.

Kain, J. S.: The Kain–Fritsch convective parameterization: An update, J. Appl. Meteorol., 43, 170–181, doi:10.1175/1520-0450(2004)043<0170:TKCPAU>2.0.CO;2, 2004.

Kalenderski, S., Stenchikov, G., and Zhao, C.: Modeling a typical winter-time dust event over the Arabian Peninsula and the Red Sea, Atmos. Chem. Phys., 13, 1999–2014, doi: 10.5194/acp-13-1999-2013, 2013.

Kalenderski, S., and Stenchikov, G.: High-resolution regional modeling of summertime transport and impact of African dust over the Red Sea and Arabian Peninsula, J. Geophys. Res.-Atmos., 121, 6435–6458, doi:10.1002/2015JD024480, 2016.

Kang, J.-Y., Yoon, S.-C., Shao, Y., and Kim, S.-W.: Comparison of vertical dust flux by implementing three dust emission schemes in WRF/Chem, J. Geophys. Res.-Atmos., 116, doi:10.1029/2010JD014649, 2011.

Kim, D., Chin, M., Bian, H., Tan, Q., Brown, M. E., Zheng, T., You, R., Diehl, T., Ginoux, P., and Kucsera, T.: The effect of the dynamic surface bareness on dust source function, emission, and distribution, J. Geophys. Res.-Atmos., 118, 871–886, doi:10.1029/2012jd017907, 2013.

Knippertz, P. and Todd, M. C.: Mineral dust aerosols over the Sahara: Meteorological controls on emission and transport and implications for modeling, Rev. Geophys., 50, RG1007, doi:10.1029/2011RG000362, 2012.

Kocha, C., Tulet, P., Lafore, J.-P. and Flamant, C.: The importance of the diurnal cycle of Aerosol Optical Depth in West Africa, Geophys. Res. Lett., 40, 785–790, doi:10.1002/grl.50143, 2013.

Koven, C. D., and Fung, I.: Identifying global dust source areas using high-resolution land surface form, J. Geophys. Res., 113, doi:10.1029/2008jd010195, 2008.

Lafon, S., Rajot, J.-L., Alfaro, S. C., and Gaudichet, A.: Quantification of iron oxides in desert aerosol, Atmos. Environ., 38, 1211–1218, doi:10.1016/j.atmosenv.2003.11.006, 2004.

Langodan, S., Cavaleri, L., Viswanadhapalli, Y. and Hoteit, I.: The Red Sea: a natural laboratory for wind and wave modeling, J. Phys. Oceanogr., 44, 3139–3159, doi:10.1175/JPO-D-13-0242.1, 2014.

Laurent, B., Marticorena, B., Bergametti, G., Léon, J. F. and Mahowald, N. M.: Modeling mineral dust emissions from the Sahara desert using new surface properties and soil database, J. Geophys. Res., 113, D14218, doi:10.1029/2007JD009484, 2008.

Lawrence, D. M., Oleson, K. W., Flanner, M. G., Thornton, P. E., Swenson, S. C., Lawrence, P. J., Zeng, X., Yang, Z.-L., Levis, S., Sakaguchi, K., Bonan, G. B. and Slater, A. G.: Parameterization improvements and functional and structural advances in Version 4 of the Community Land Model, J. Adv. Model. Earth Syst., 3, M03001, doi:10.1029/2011MS000045, 2011.

Lin, Y.-L., Farley, R. D. and Orville, H. D.: Bulk parameterization of the snow field in a cloud model, J. Clim. Appl. Meteorol., 22, 1065–1092, doi:10.1175/1520-0450(1983)022<1065:BPOTSF>2.0.CO;2, 1983.

Mahowald, N., S. Engelstaedter, C. Luo, A. Sealy, P. Artaxo, C. Benitez-Nelson, S. Bonnet, Y. Chen, P.Y. Chuang, D.D. Cohen, F. Dulac, B. Herut, A.M. Johansen, N. Kubilay, R. Losno, W. Maenhaut, A. Paytan, J.M. Prospero, L.M. Shank, and

R.L. Siefert: Atmospheric iron deposition: Global distribution, variability and human perturbations, Ann. Rev. Marine Sci., 1, 245–278, 2009.

Mahowald, N. M., Baker, A. R., Bergametti, G., Brooks, N., Duce, R. A., Jickells, T. D., Kubilay, N., Prospero, J. M. and Tegen, I.: Atmospheric global dust cycle and iron inputs to the ocean, Global Biogeochem. Cycles, 19, doi:10.1029/2004GB002402, 2005.

Mahowald, N. M., Muhs, D. R., Levis, S., Rasch, P. J., Yoshioka, M., Zender, C. S., and Luo, C.: Change in atmospheric mineral aerosols in response to climate: Last glacial period, preindustrial, modern, and doubled carbon dioxide climates, J. Geophys. Res.-Atmos., 111, doi:10.1029/2005JD006653, 2006.

Mahowald, N. M., Ballantine, J. A., Feddema, J., and Ramankutty, N.: Global trends in visibility: implications for dust sources, Atmos. Chem. Phys., 7, 3309–3339, doi:10.5194/acp-7-3309-2007, 2007.

Marticorena, B. and Bergametti, G.: Modeling the atmospheric dust cycle: 1. Design of a soil-derived dust emission scheme, J. Geophys. Res., 100, 16415, doi:10.1029/95JD00690, 1995.

Menut, L., Pérez, C., Haustein, K., Bessagnet, B., Prigent, C., and Alfaro, S.: Impact of surface roughness and soil texture on mineral dust emission fluxes modeling, J. Geophys. Res.-Atmos., 118, 6505–6520, doi:10.1002/jgrd.50313, 2013.

Miller, R. L., Knippertz, P., Pérez García-Pando, C., Perlwitz, J. P. and Tegen, I.: Impact of Dust Radiative Forcing upon Climate, in Mineral dust: A key player in the Earth system, edited by P. Knippertz and J.-B. W. Stuut, pp. 327–357, Springer Netherlands, Dordrecht., 2014.

Mlawer, E. J., Taubman, S. J., Brown, P. D., Iacono, M. J. and Clough, S. A.: Radiative transfer for inhomogeneous atmospheres: RRTM, a validated correlated-k model for the longwave, J. Geophys. Res.-Atmos., 102, 16663–16682, doi:10.1029/97JD00237, 1997.

Morman, S. A. and Plumlee, G. S.: Dust and Human Health, in Mineral dust: A key player in the Earth system, edited by P. Knippertz and J.-B. W. Stuut, pp. 385–409, Springer Netherlands, Dordrecht., 2014.

Nickovic, S., Vukovic, A., Vujadinovic, M., Djurdjevic, V., and Pejanovic, G.: Technical Note: High-resolution mineralogical database of dust-productive soils for atmospheric dust modeling, Atmos. Chem. Phys., 12, 845–855, 2012.

Nickovic, S., Vukovic, A., and Vujadinovic, M.: Atmospheric processing of iron carried by mineral dust, Atmos. Chem. Phys., 13, 9169–9181, doi:10.5194/acp-13-9169-2013, 2013.

Notaro, M., Alkolibi, F., Fadda, E. and Bakhrjy, F.: Trajectory analysis of Saudi Arabian dust storms, J. Geophys. Res. Atmos., 118, 6028–6043, doi:10.1002/jgrd.50346, 2013.

Notaro, M., Yu, Y. and Kalashnikova, O. V.: Regime shift in Arabian dust activity, triggered by persistent Fertile Crescent drought, J. Geophys. Res. Atmos., 120, 10229–10249, doi:10.1002/2015JD023855, 2015.

Okin, G. S., Baker, A. R., Tegen, I., Mahowald, N. M., Dentener, F. J., Duce, R. A., Galloway, J. N., Hunter, K., Kanakidou, M., Kubilay, N., Prospero, J. M., Sarin, M., Surapipith, V., Uematsu, M. and Zhu, T.: Impacts of atmospheric nutrient deposition on marine productivity: Roles of nitrogen, phosphorus, and iron, Global Biogeochem. Cycles, 25, doi:10.1029/2010GB003858, 2011.

Oleson, K. W., Lawrence, D. M., Bonan, G. B., Flanner, M. G., Kluzek, E., Lawrence, P. J., Levis, S., Swenson, S. C., Thornton, P. E., Dai, A., Decker, M., Dickinson, R., Feddema, J., Heald, C. L., Hoffman, F., Lamarque, J., Mahowald, N., Niu, G., Qian, T., Randerson, J., Running, S., Sakaguchi, K., Slater, A., Stockli, R., Wang, A., Yang, Z., Zeng, X., and Zeng, X.: Technical description of version 4.0 of the Community Land Model (CLM), NCAR Tech. Note, NCAR/TN-478+STR, NCAR, Boulder, 2010.

Osipov, S., Stenchikov, G., Brindley, H., and Banks, J.: Diurnal cycle of the dust instantaneous direct radiative forcing over the Arabian Peninsula, Atmos. Chem. Phys., 15, 9537–9553, doi:10.5194/acp-15-9537-2015, 2015.

Parajuli, S. P., Yang, Z.-L., and Kocurek, G.: Mapping erodibility in dust source regions based on geomorphology, meteorology, and remote sensing, J. Geophys. Res.-Earth Surf., 119, 1977–1994, doi:10.1002/2014JF003095, 2014.

Pérez, C., Haustein, K., Janjic, Z., Jorba, O., Huneeus, N., Baldasano, J. M., Black, T., Basart, S., Nickovic, S., Miller, R. L., Perlwitz, J. P., Schulz, M., and Thomson, M.: Atmospheric dust modeling from meso to global scales with the online NMMB/BSC-Dust model – Part 1: Model description, annual simulations and evaluation, Atmos. Chem. Phys., 11, 13001–13027, doi:10.5194/acp-11-13001-2011, 2011.

Perlwitz, J. P., Pérez García-Pando, C., and Miller, R. L.: Predicting the mineral composition of dust aerosols – Part 1: Representing key processes, Atmos. Chem. Phys., 15, 11593–11627, doi:10.5194/acp-15-11593-2015, 2015.

Prakash, P. J., Stenchikov, G., Kalenderski, S., Osipov, S., and Bangalath, H.: The impact of dust storms on the Arabian Peninsula and the Red Sea, Atmos. Chem. Phys., 15, 199–222, doi:10.5194/acp-15-199-2015, 2015.

Prakash, P. J., Stenchikov, G., Tao, W., Yapici, T., Warsama, B. and Engelbrecht, J. P.: Arabian Red Sea coastal soils as potential mineral dust sources, Atmos. Chem. Phys., 16, 11991–12004, doi:10.5194/acp-16-11991-2016, 2016.

Prospero, J. M., Ginoux, P., Torres, O., Nicholson, S. E., and Gill, T. E.: Environmental characterization of global sources of atmospheric soil dust indentified with the NIMBUS 7 total ozone mapping spectrometer (TOMS) absorbing aerosol product, Rev. Geophys., 40, 1–31, doi:10.1029/2000RG000095, 2002.

Raupach, M. and Lu, H.: Representation of land-surface processes in aeolian transport models, Environ. Model. Softw., 19, 93–112, doi:10.1016/S1364-8152(03)00113-0, 2004.

Rezazadeh, M., Irannejad, P. and Shao, Y.: Climatology of the Middle East dust events, Aeolian Res., 10, 103–109, doi:10.1016/j.aeolia.2013.04.001, 2013.

Ridley, D. A., Heald, C. L., Kok, J. F. and Zhao, C.: An observationally constrained estimate of global dust aerosol optical depth, Atmos. Chem. Phys., 16, 15097–15117, doi:10.5194/acp-16-15097-2016, 2016.

Rienecker, M. M., Suarez, M. J., Gelaro, R., Todling, R., Bacmeister, J., Liu, E., Bosilovich, M. G., Schubert, S. D., Takacs, L., Kim, G.-K., Bloom, S., Chen, J., Collins, D., Conaty, A., da Silva, A., Gu, W., Joiner, J., Koster, R. D., Lucchesi, R., Molod, A., Owens, T., Pawson, S., Pegion, P., Redder, C. R., Reichle, R., Robertson, F. R., Ruddick, A. G., Sienkiewicz, M. and Woollen, J.: MERRA: NASA's Modern-Era Retrospective Analysis for Research and Applications, J. Clim., 24(14), 3624–3648, doi:10.1175/JCLI-D-11-00015.1, 2011.

Scanza, R. A., Mahowald, N., Ghan, S., Zender, C. S., Kok, J. F., Liu, X., Zhang, Y. and Albani, S.: Modeling dust as component minerals in the Community Atmosphere Model: development of framework and impact on radiative forcing, Atmos. Chem. Phys., 15, 537–561, doi:10.5194/acp-15-537-2015, 2015.

Schepanski, K., Tegen, I. and Macke, A.: Comparison of satellite based observations of Saharan dust source areas, Remote Sens. Environ., 123, 90–97, doi:10.1016/j.rse.2012.03.019, 2012.

Schulz, M., Prospero, J. M., Baker, A. R., Dentener, F., Ickes, L., Liss, P. S., Mahowald, N. M., Nickovic, S., García-Pando, C. P., Rodríguez, S., Sarin, M., Tegen, I., and Duce, R. A.: Atmospheric transport and deposition of mineral dust to the ocean: Implications for research needs, Environ. Sci. Technol., 46, 10390–10404, doi:10.1021/es300073u, 2012.

Shalaby, A., Rappenglueck, B., and Eltahir, E. A. B.: The climatology of dust aerosol over the Arabian Peninsula, Atmos. Chem. Phys. Discuss., 2015, 1523–1571, doi:10.5194/acpd-15-1523-2015, 2015.

Shao, Y.: A model for mineral dust emission, J. Geophys. Res. Atmos., 106(D17), 20239–20254, doi:10.1029/2001JD900171, 2001.

Shao, Y., Yang, Y., Wang, J., Song, Z., Leslie, L. M., Dong, C., Zhang, Z., Lin, Z., Kanai, Y., Yabuki, S., and Chun, Y.: Northeast Asian dust storms: Real-time numerical prediction and validation, J. Geophys. Res.-Atmos., 108, doi:10.1029/2003JD003667, 2003.

Shao, Y.: Simplification of a dust emission scheme and comparison with data, J. Geophys. Res.-Atmos., 109, 372, doi:10.1029/2003JD004372, 2004.

Shao, Y. and Dong, C. H.: A review on East Asian dust storm climate, modelling and monitoring, Glob. Planet. Change, 52, 1–22, doi:10.1016/j.gloplacha.2006.02.011, 2006.

Shao, Y.: Physics and modelling of wind erosion, Springer Netherlands, Dordrecht, 2008.

Shao, Y., Wyrwoll, K.-H., Chappell, A., Huang, J., Lin, Z., McTainsh, G. H., Mikami, M., Tanaka, T. Y., Wang, X., and Yoon, S.: Dust cycle: An emerging core theme in Earth system science, Aeolian Res., 2, 181–204, doi:10.1016/j.aeolia.2011.02.001, 2011a.

Shao, Y., Ishizuka, M., Mikami, M., and Leys, J. F.: Parameterization of size-resolved dust emission and validation with measurements, J. Geophys. Res.-Atmos., 116, doi:10.1029/2010JD014527, 2011b.

Shi, M., Yang, Z.-L., Stenchikov, G. L., Parajuli, S. P., Tao, W. and Kalenderski, S.: Quantifying the impacts of landscape heterogeneity and model resolution on dust emissions in the Arabian Peninsula, Environ. Model. Softw., 78, 106–119, doi:10.1016/j.envsoft.2015.12.021, 2016.

Singh, R. P., Prasad, A. K., Kayetha, V. K. and Kafatos, M.: Enhancement of oceanic parameters associated with dust storms using satellite data, J. Geophys. Res., 113, C11008, doi:10.1029/2008JC004815, 2008.

Skamarock, W. C., Klemp, J. B., Dudhia, J., Gill, D. O., Barker, D. M., Wang, W., and Powers, J. G.: A description of the advanced research WRF version 2, NCAR Tech. Note, NCAR/TN-468+STR, NCAR, Boulder, 2008.

Smith, A., Lott, N., and Vose, R.: The Integrated Surface Database: Recent developments and partnerships, Bulletin of the American Meteorological Society, 92, 704–708, doi:10.1175/2011BAMS3015.1, 2011.

Tegen, I., and Fung, I.: Modeling of mineral dust in the atmosphere: Sources, transport, and optical thickness, J. Geophys. Res.-Atmos., 99, 22897–22914, doi:10.1029/94JD01928, 1994.

Tegen, I.: Modeling the mineral dust aerosol cycle in the climate system, Quat. Sci. Rev., 22, 1821–1834, doi:10.1016/S0277-3791(03)00163-X, 2003.

Tewari, M., Chen, F., Wang, W., Dudhia, J., LeMone, M. A., Mitchell, K., Ek, M., Gayno, G., Wegiel, J., and Cuenca, R. H.: Implementation and verification of the unified NOAH land surface model in the WRF model, 20th conference on weather analysis and forecasting/16th conference on numerical weather prediction, Boulder, USA, 22–25 June 2004, 11–15, 2004.

Textor, C., Schulz, M., Guibert, S., Kinne, S., Balkanski, Y., Bauer, S., Berntsen, T., Berglen, T., Boucher, O., Chin, M., Dentener, F., Diehl, T., Easter, R., Feichter, H., Fillmore, D., Ghan, S., Ginoux, P., Gong, S., Grini, A., Hendricks, J., Horowitz, L., Huang, P., Isaksen, I., Iversen, I., Kloster, S., Koch, D., Kirkevåg, A., Kristjansson, J. E., Krol, M., Lauer, A., Lamarque, J. F., Liu, X., Montanaro, V., Myhre, G., Penner, J., Pitari, G., Reddy, S., Seland, Ø., Stier, P., Takemura, T., and Tie, X.: Analysis and quantification of the diversities of aerosol life cycles within AeroCom, Atmos. Chem. Phys., 6, 1777–1813, doi:10.5194/acp-6-1777-2006, 2006.

Todd, M. C., Bou Karam, D., Cavazos, C., Bouet, C., Heinold, B., Baldasano, J. M., Cautenet, G., Koren, I., Perez, C., Solmon, F., Tegen, I., Tulet, P., Washington, R. and Zakey, A.: Quantifying uncertainty in estimates of mineral dust flux: An intercomparison of model performance over the Bodélé Depression, northern Chad, J. Geophys. Res., 113, D24107, doi:10.1029/2008JD010476, 2008.

Vincent, P.: Saudi Arabia: An Environmental Overview., Taylor & Francis, Leiden, The Netherlands, 2008.

de Vries, A. J., Feldstein, S. B., Riemer, M., Tyrlis, E., Sprenger, M., Baumgart, M., Fnais, M. and Lelieveld, J.: Dynamics of tropical-extratropical interactions and extreme precipitation events in Saudi Arabia in autumn, winter and spring, Q. J. R. Meteorol. Soc., 142, 1862–1880, doi:10.1002/qj.2781, 2016.

Walker, A. L., Liu, M., Miller, S. D., Richardson, K. A. and Westphal, D. L.: Development of a dust source database for mesoscale forecasting in southwest Asia, J. Geophys. Res., 114, D18207, doi:10.1029/2008JD011541, 2009.

Wang, G., Yu, M., Pal, J. S., Mei, R., Bonan, G. B., Levis, S. and Thornton, P. E.: On the development of a coupled regional climate–vegetation model RCM–CLM–CN–DV and its validation in Tropical Africa, Clim. Dyn., 46, 515–539, doi:10.1007/s00382-015-2596-z, 2016.

Wang, Y., Stein, A. F., Draxler, R. R., de la Rosa, J. D., and Zhang, X.: Global sand and dust storms in 2008: Observation and HYSPLIT model verification, Atmos. Environ., 45, 6368–6381, doi:10.1016/j.atmosenv.2011.08.035, 2011.

Washington, R., Todd, M., Middleton, N. J., and Goudie, A. S.: Dust-storm source areas determined by the total ozone monitoring spectrometer and surface observations, Ann. Assoc. Amer. Geograph., 93, 297–313, doi:10.1111/1467-8306.9302003, 2003.

Webb, N. P., and Strong, C. L.: Soil erodibility dynamics and its representation for wind erosion and dust emission models, Aeolian Res., 3, 165–179, doi:10.1016/j.aeolia.2011.03.002, 2011.

Weikert, H.: Plankton and the pelagic environment in: Key environments: Red Sea, edited by: Edwards, A. J., and Head, S. M., Pergamon Press, Oxford, 90–111, 1987.

Yu, Y., Notaro, M., Liu, Z., Kalashnikova, O., Alkolibi, F., Fadda, E., and Bakhrjy, F.: Assessing temporal and spatial variations in atmospheric dust over Saudi Arabia through satellite, radiometric, and station data, J. Geophys. Res.-Atmos., 118, 13253–13264, doi:10.1002/2013jd020677, 2013.

Yu, Y., Notaro, M., Liu, Z., Wang, F., Alkolibi, F., Fadda, E., and Bakhrjy, F.: Climatic controls on the interannual to decadal variability in Saudi Arabian dust activity: Toward the development of a seasonal dust prediction model, J. Geophys. Res.-Atmos., 120, 1739–1758, doi:10.1002/2014JD022611, 2015.

Zaveri, R. A. and Peters, L. K.: A new lumped structure photochemical mechanism for large-scale applications, J. Geophys. Res., 104, 30387–30415, doi: 10.1029/2007JD008782, 1999.

Zaveri, R. A., Easter, R. C., Fast, J. D., and Peters, L. K.: Model for simulating aerosol interactions and chemistry (MOSAIC), J. Geophys. Res., 113, D13204, doi:10.1029/2007JD008792, 2008.

Zender, C. S., Huisheng, B., and David, N.: Mineral Dust Entrainment and Deposition (DEAD) model: Description and 1990s dust climatology, J. Geophys. Res.-Atmos., 108, 4416, doi:10.1029/2002JD002775, 2003a.

Zender, C. S., Newman, D., and Torres, O.: Spatial heterogeneity in aeolian erodibility: Uniform, topographic, geomorphic, and hydrologic hypotheses, J. Geophys. Res.-Atmos., 108, doi:10.1029/2002JD003039, 2003b.

Zhang, Y., Mahowald, N., Scanza, R. A., Journet, E., Desboeufs, K., Albani, S., Kok, J. F., Zhuang, G., Chen, Y., Cohen, D. D., Paytan, A., Patey, M. D., Achterberg, E. P., Engelbrecht, J. P., and Fomba, K. W.: Modeling the global emission, transport and deposition of trace elements associated with mineral dust, Biogeosciences, 12, 5771–5792, doi:10.5194/bg-12-5771-2015, 2015.

Zhao, C., Liu, X., Leung, L. R., Johnson, B., McFarlane, S. A., Gustafson Jr, W. I., Fast, J. D., and Easter, R.: The spatial distribution of mineral dust and its shortwave radiative forcing over North Africa: modeling sensitivities to dust emissions and aerosol size treatments, Atmos. Chem. Phys., 10, 8821–8838, doi:10.5194/acp-10-8821-2010, 2010.

Zhao, C., Chen, S., Leung, L. R., Qian, Y., Kok, J. F., Zaveri, R. A., and Huang, J.: Uncertainty in modeling dust mass balance and radiative forcing from size parameterization, Atmos. Chem. Phys., 13, 10733–10753, doi:10.5194/acp-13-10733-2013, 2013.

Zhao, C., Huang, M., Fast, J. D., Berg, L. K., Qian, Y., Guenther, A., Gu, D., Shrivastava, M., Liu, Y., Walters, S., Pfister, G., Jin, J., Shilling, J. E., and Warneke, C.: Sensitivity of biogenic volatile organic compounds to land surface parameterizations and vegetation distributions in California, Geosci. Model Dev., 9, 1959–1976, doi:10.5194/gmd-9-1959-2016, 2016.

Table 1. WRF model configuration.

Process	**WRF Option**
Microphysics	Lin (Lin et al., 1983)
Shortwave radiation	Goddard (Chou and Suarez, 1999)
Longwave radiation	RRTM (Mlawer et al., 1997)
Cumulus parameterization	Kain-Fritsch (Kain, 2004)
Surface layer	Monin-Obukhov (Janjić, 1994)
Land-surface model	Noah LSM (Tewari et al., 2004)
Boundary layer scheme	YSU (Hong et al., 2006)
Boundary and initial conditions	NCEP Final Analysis FNL
Sea Surface Temperature	NCEP RTG_SST_HR

Table 2. Land surface data used in model setup.

Input data	Parameters affected	Default data in CLM4	Data used	
		Resolution	Original data Resolution	Source
PFT	f_m	0.5° × 0.5°	500m × 500m	MODIS Land Cover Product MYD12
LAI			1km × 1km	MODIS MCD15
SAI			1km × 1km	Calculated from LAI
CLY	α_j, f_w		1km × 1km	STATSGO-FAO (10km × 10km)
ERD	S	Constant=1	See Table 4	

Table 3. Spatial resolution of input datasets used in simulations.

		Simulation					
		10kmALL	50kmALL	1kmALL	10kmLPFT	10kmLLAI	10kmLCLY
Input data	PFT	10 km	50 km	1 km	50 km	10 km	10 km
	LAI & SAI	10 km	50 km	1 km	10 km	50 km	10 km
	CLY	10 km	50 km	1 km	10 km	10 km	50 km
	Wind forcing	10 km					

Table 4. Tuning constants used in the simulations

Source function	Algorithm	T in (1)	Data source	Remarks
No source function	Eq. (1), $S = 1$	0.011	Calculated based on 10kmALL experiment	Used in 50kmALL, 10kmLPFT, 10kmLLAI, 10kmLCLY, 10kmALL and 1kmALL experiments.
SEVIRI statistical	Eq. (3)	1.28	SEVIRI AOD data (Brindley and Russell, 2009; Banks and Brindley, 2013)	Used in 1kmALL simulation with SEVIRI source function.

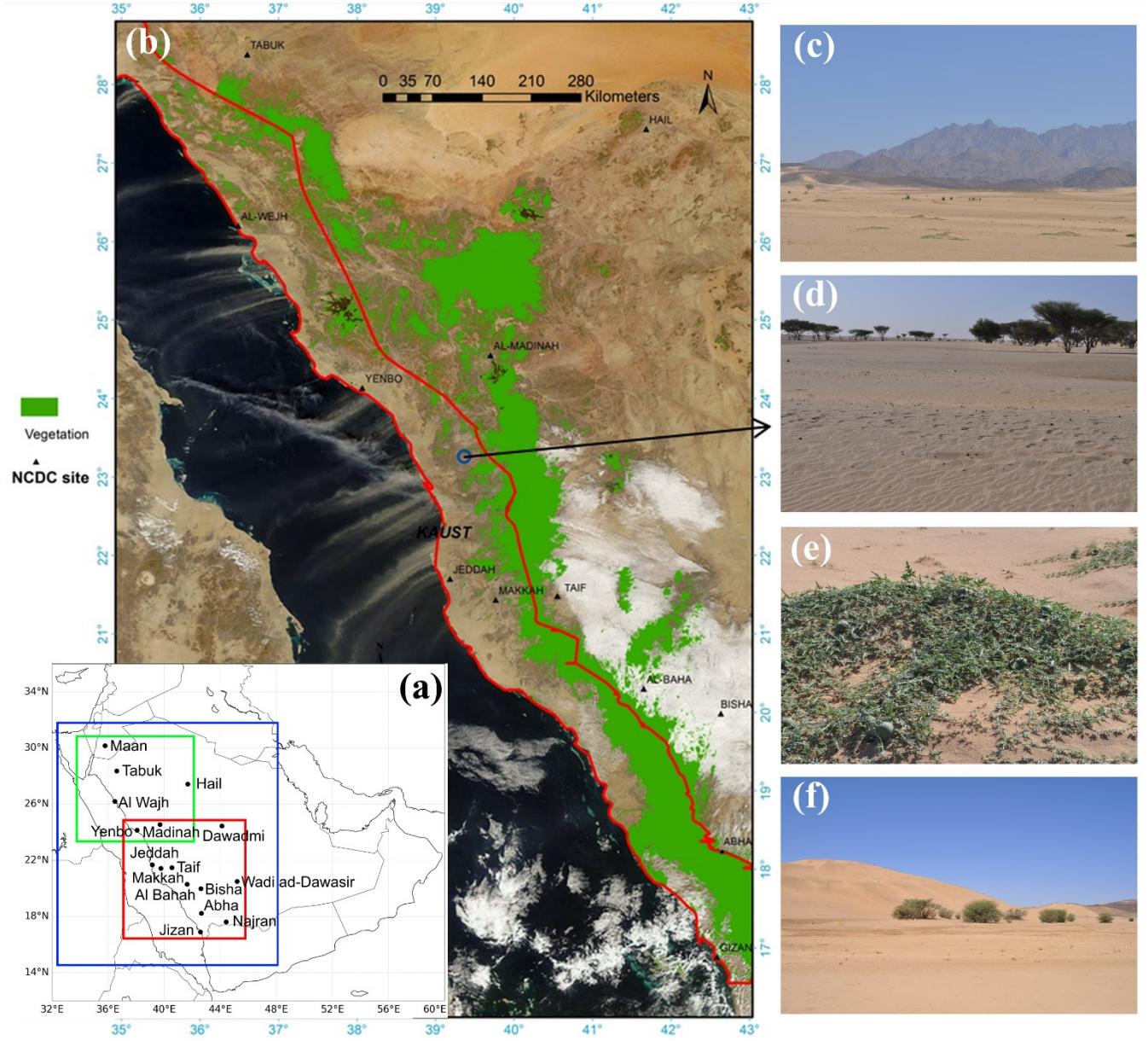

Figure 1. (a) The CLM4 model domains (green and red), WRF-Chem domain (blue), and 16 ground observation stations. (b) Dust plume above the Red Sea observed by MODIS/TERRA at 7:45 UTC on 14 January 2009. Overview of the landscapes: (c) piedmont; (d) trees over the sand; (e) wild watermelons over the sand; (f) sand dunes and scattered vegetation.

5

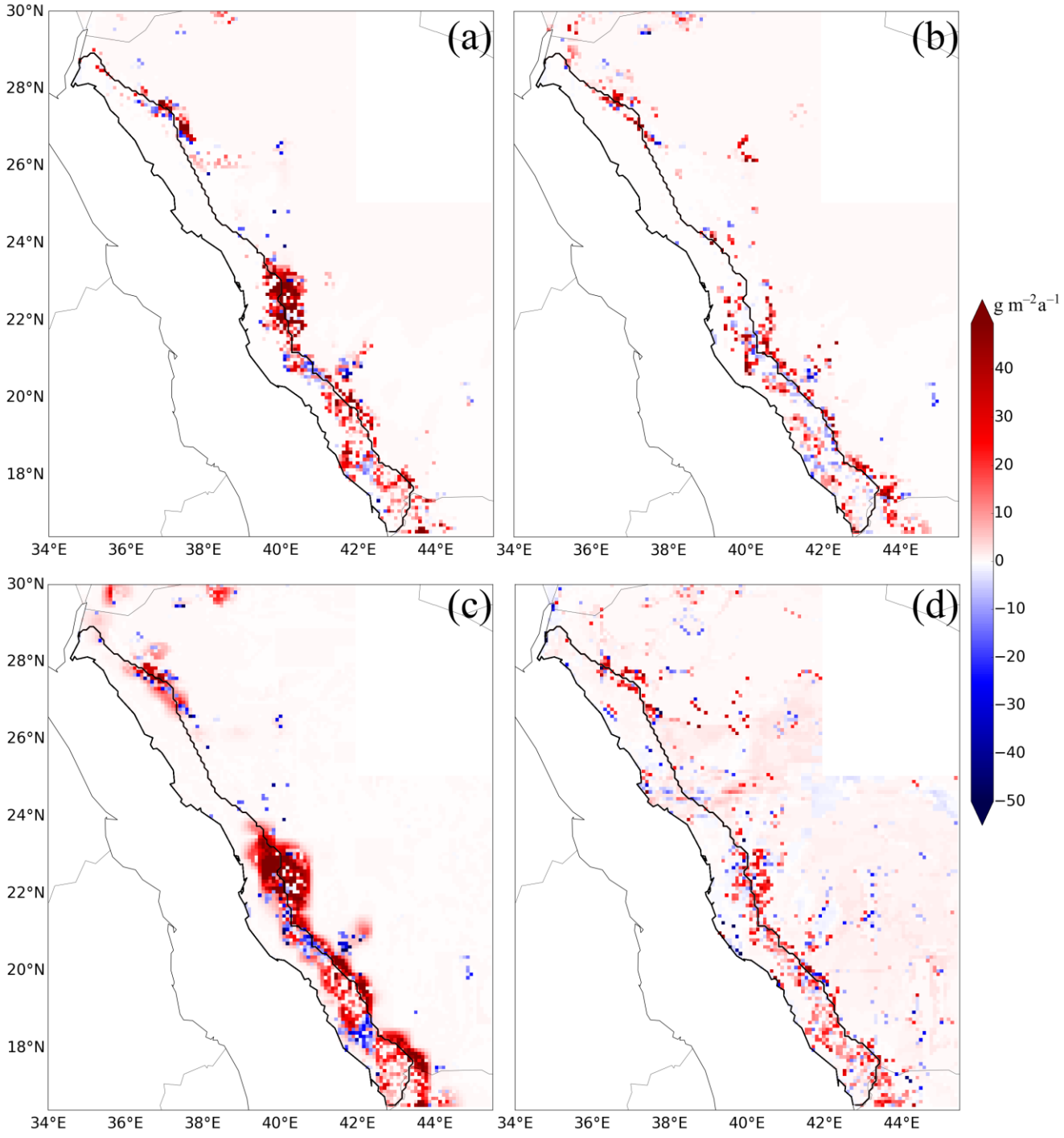

Figure 2. Differences between annual mean dust emission in model simulations (g m^{-2} a^{-1}): (a) 10kmALL – 10kmLLAI; (b) 10kmALL – 10kmLPFT; (c) 10kmALL – 50kmALL; (d) 1kmALL – 10kmALL.

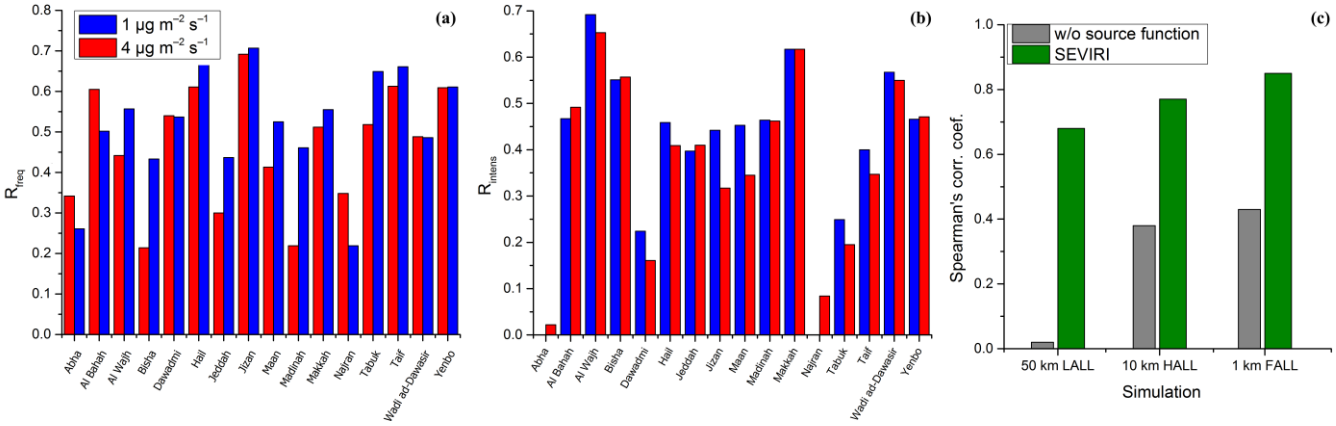

Figure 3. Spearman's correlation coefficients for monthly-mean series of (a) dust event frequency and (b) intensity between station data and results from 10kmALL experiment. (c) Spatial metrics of model performance (see text for definition) for three basic experiments with and without SEVIRI source function.

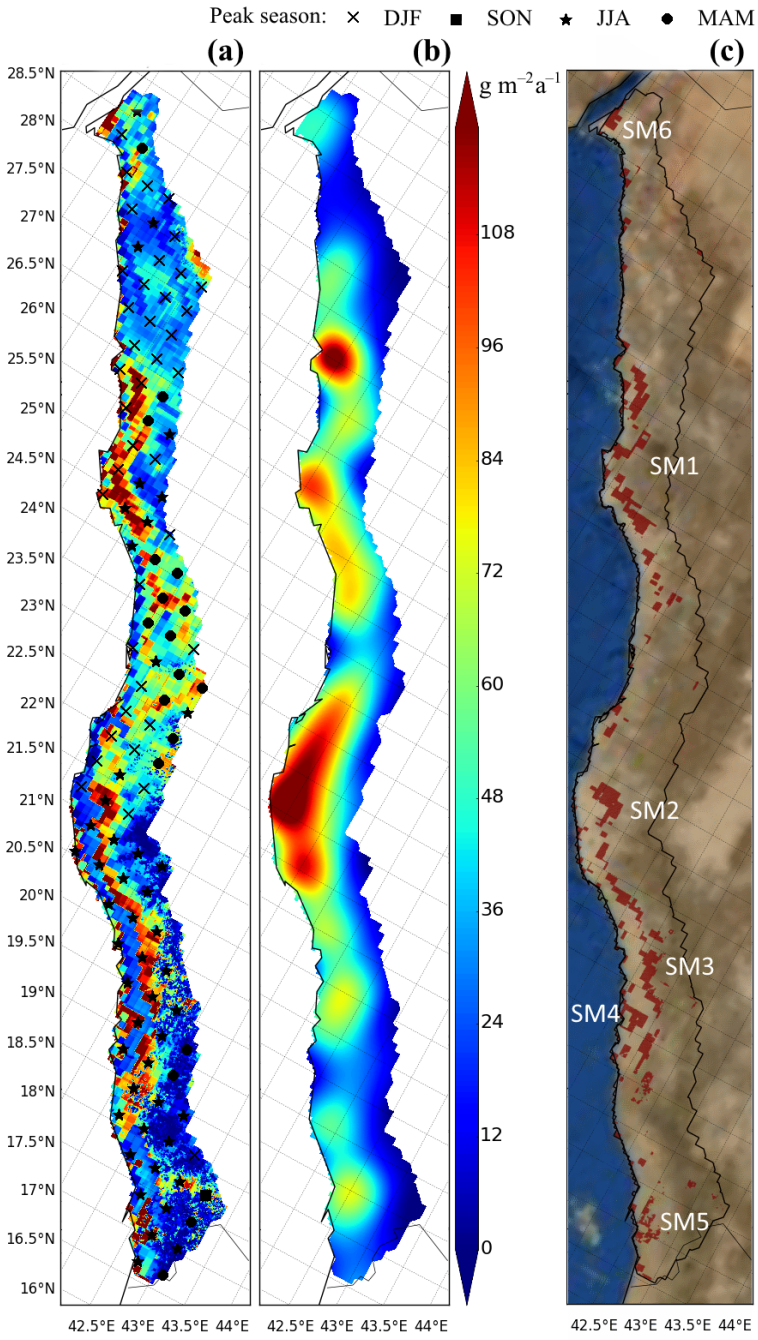

Figure 4. Annual dust emission (g m^{-2} a^{-1}) in (a) 1kmALL experiment with SEVIRI source function (2009–2011); (b) MERRAero reanalysis (2003–2015). (c) Main dust emission hot spot areas mapped on real color satellite image. Peak season is shown by marks (see figure legend).

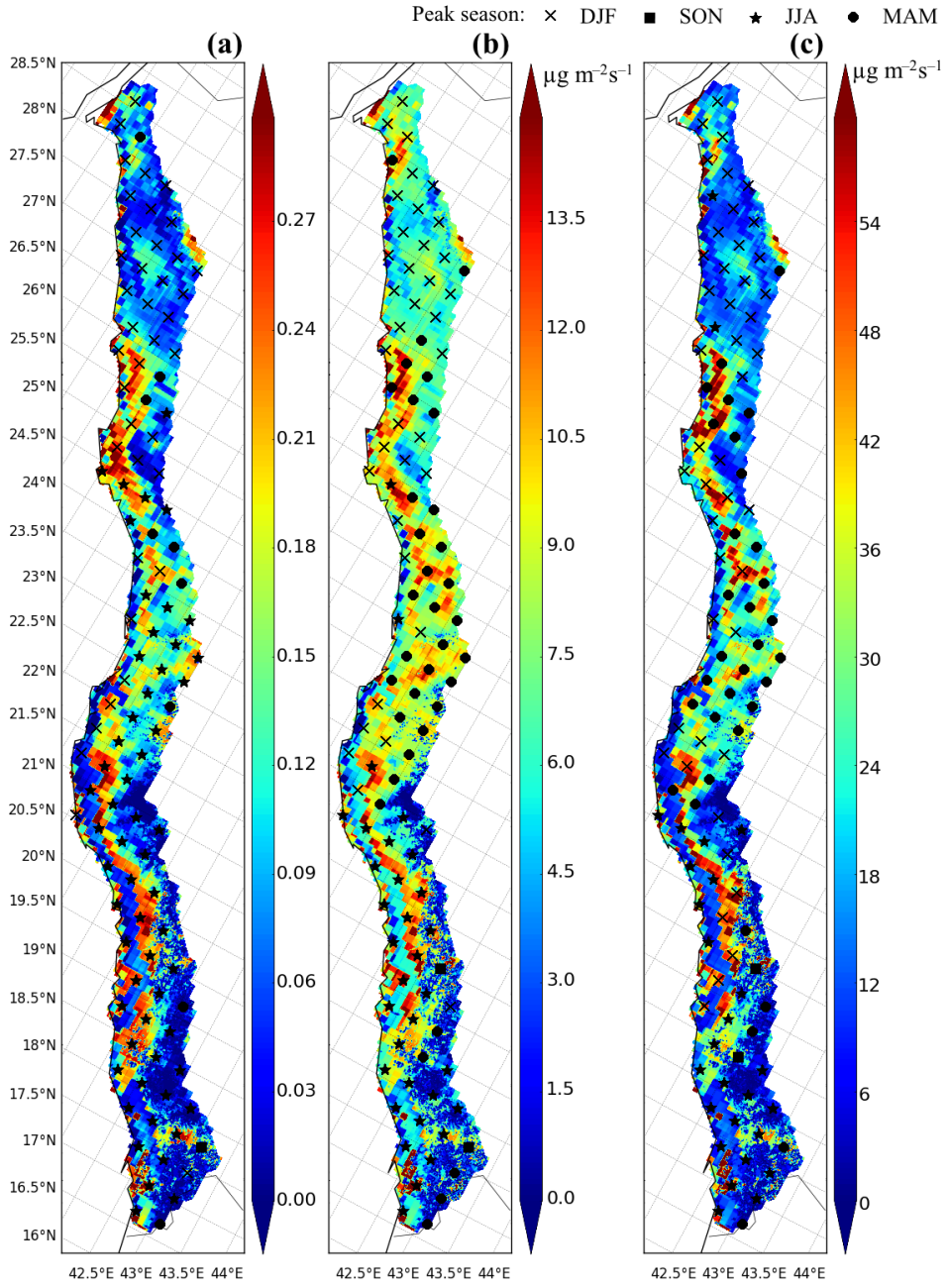

Figure 5. Average 2009–2011 (a) dust event frequency; (b) average emission intensity (µg m^{-2} s^{-1}); (c) yearly maximum emission rate (µg m^{-2} s^{-1}) in 1kmALL experiment with SEVIRI source function. Peak season is shown by marks (see figure legend).

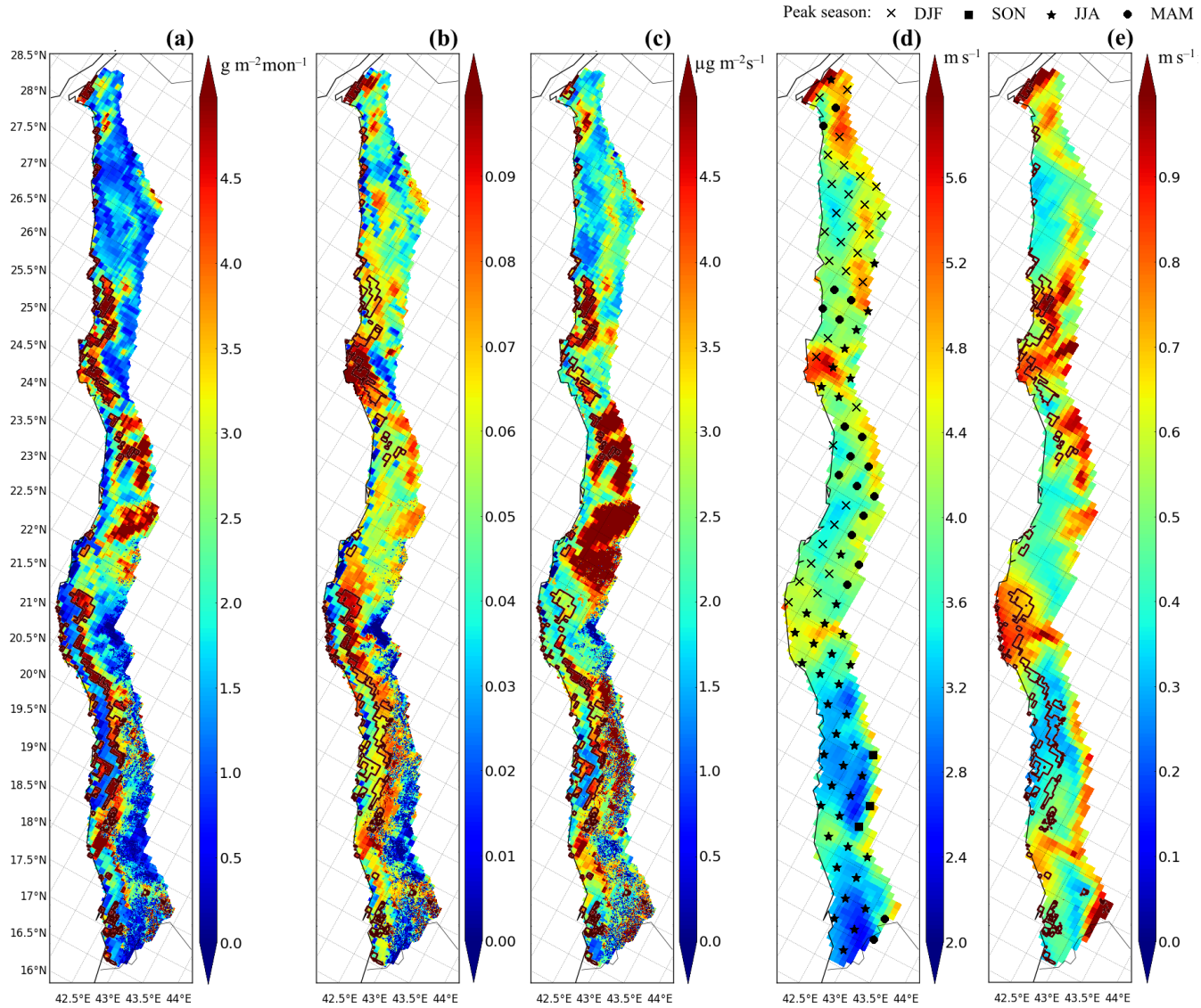

Figure 6. Standard deviations of monthly (a) total dust emission (g m^{-2} mon^{-1}); (b) dust event frequency; (c) average emission intensity (μg m^{-2} s^{-1}) in 1kmALL experiment with SEVIRI source function. Average 2009–2011 WRF forcing (d) wind speed (m s^{-1}), and (e) its monthly standard deviation (m s^{-1}). Peak season is shown by marks (see figure legend).

5

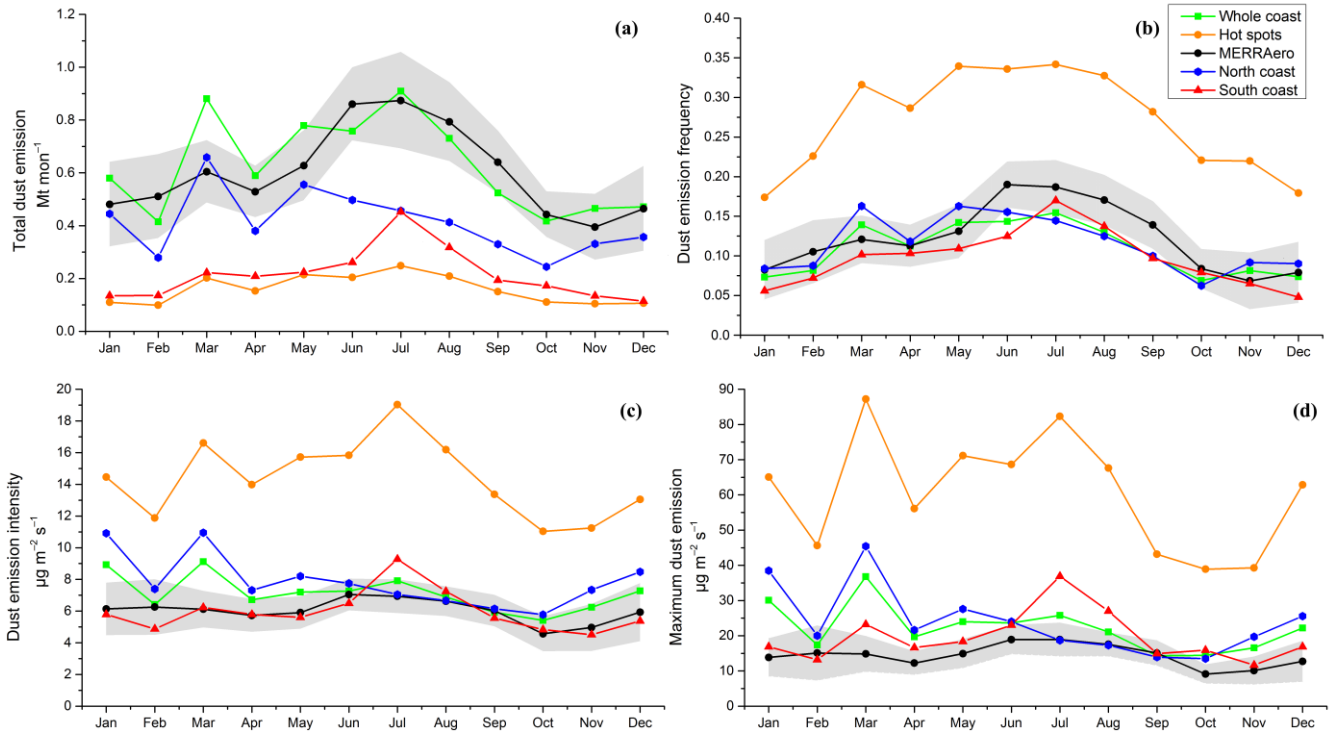

Figure 7. Average seasonal cycles of monthly (a) total dust emission (Mt mon^{-1}); (b) dust event frequency; (c) average emission intensity (μg m^{-2} s^{-1}); (d) maximum emission rate (μg m^{-2} s^{-1}) in 1kmALL experiment with SEVIRI source function (2009–2011) and MERRAero reanalysis (2003–2015). MERRAero Standard deviation intervals are shown by shading.

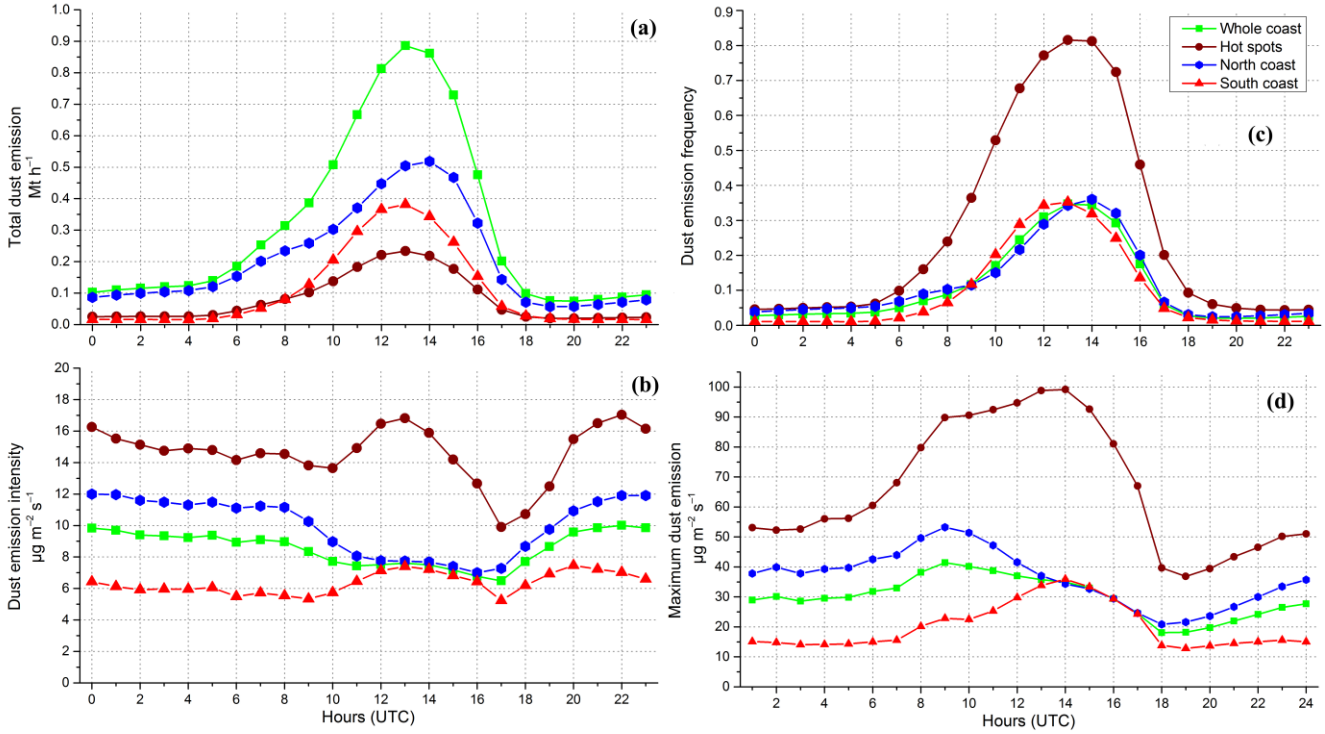

Figure 8. Annual mean diurnal cycles of (a) total dust emission (Mt h^{-1}); (b) dust event frequency; (c) average emission intensity (μg m^{-2} s^{-1}); (d) maximum emission rate (μg m^{-2} s^{-1}) in 1kmALL experiment with SEVIRI source function (2009–2011).

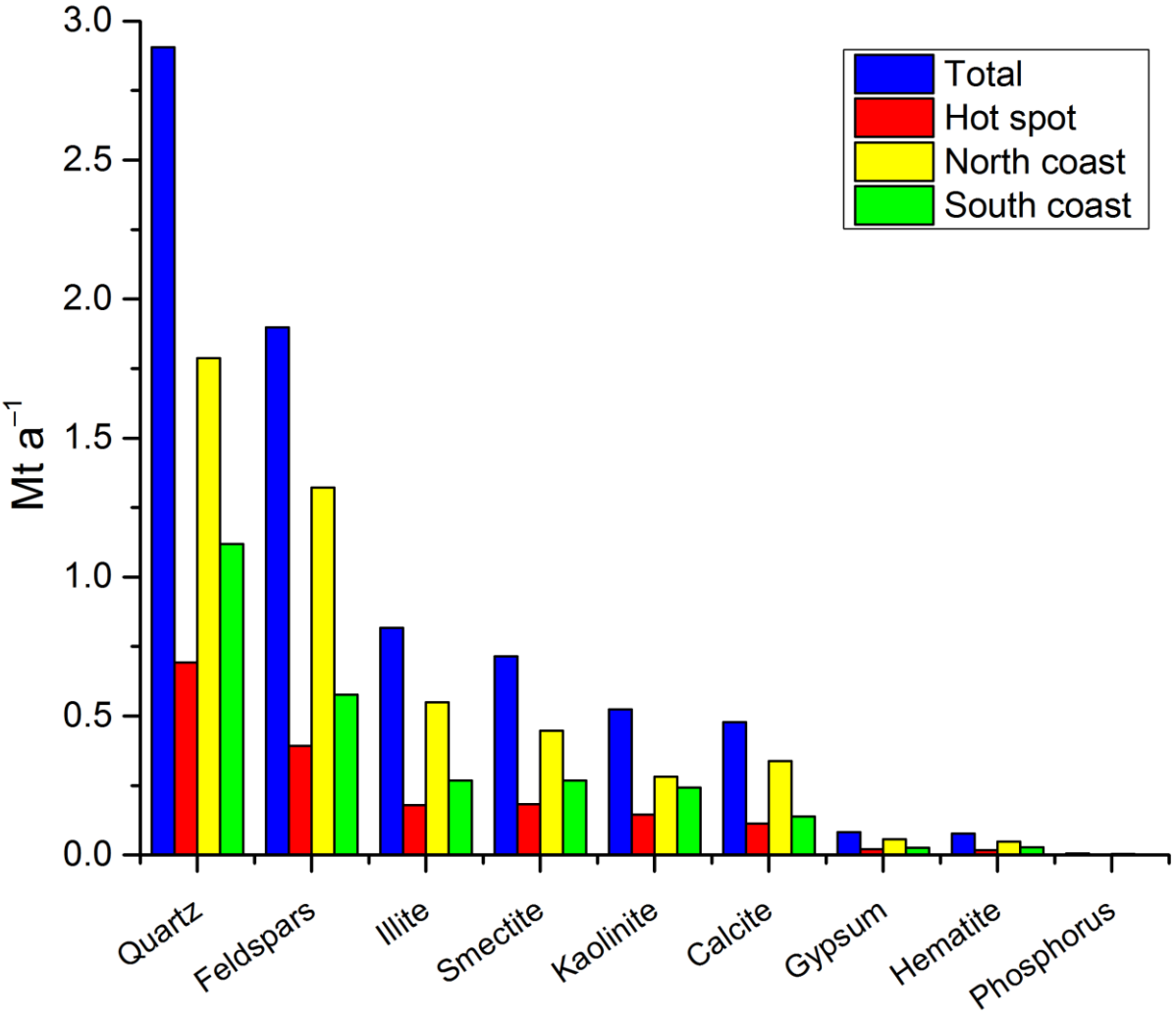

Figure 9. Annual mineral emission fluxes (Mt a^{-1}) in 1kmALL experiment with SEVIRI source function (2009–2011).